



HAL
open science

Porous polycrystal plasticity modeling of neutron-irradiated austenitic stainless steels

Pierre Guy Vincent, Hervé Moulinec, Louis Joëssel, Martin Idiart, Mihai
Garajeu

► **To cite this version:**

Pierre Guy Vincent, Hervé Moulinec, Louis Joëssel, Martin Idiart, Mihai Garajeu. Porous polycrystal plasticity modeling of neutron-irradiated austenitic stainless steels. *Journal of Nuclear Materials*, 2020, 542, pp.152463. 10.1016/j.jnucmat.2020.152463 . hal-03096211

HAL Id: hal-03096211

<https://hal.science/hal-03096211>

Submitted on 4 Jan 2021

HAL is a multi-disciplinary open access archive for the deposit and dissemination of scientific research documents, whether they are published or not. The documents may come from teaching and research institutions in France or abroad, or from public or private research centers.

L'archive ouverte pluridisciplinaire **HAL**, est destinée au dépôt et à la diffusion de documents scientifiques de niveau recherche, publiés ou non, émanant des établissements d'enseignement et de recherche français ou étrangers, des laboratoires publics ou privés.



Distributed under a Creative Commons Attribution - NonCommercial - NoDerivatives 4.0
International License

Porous polycrystal plasticity modeling of neutron-irradiated austenitic stainless steels

Pierre-Guy Vincent^{a,*}, Hervé Moulinec^b, Louis Joëssel^a, Martín I. Idiart^{c,d}, Mihail Găărăjeu^b

^a*Institut de Radioprotection et de Sûreté Nucléaire, B.P. 3, 13115 Saint-Paul-lez-Durance Cedex, France*

^b*Aix-Marseille Univ, CNRS, Centrale Marseille, LMA, 4 Impasse Nikola Tesla, CS 40006, 13453 Marseille Cedex 13, France*

^c*Centro Tecnológico Aeroespacial / Departamento de Aeronáutica, Facultad de Ingeniería, Universidad Nacional de La Plata
Avda. 1 esq. 47 S/N, La Plata B1900TAG, Argentina*

^d*Consejo Nacional de Investigaciones Científicas y Técnicas (CONICET)
CCT La Plata, Calle 8 N 1467, La Plata B1904CMC, Argentina*

Abstract

A micromechanical model for quantifying the simultaneous influence of irradiation hardening and swelling on the mechanical stiffness and strength of neutron-irradiated austenitic stainless steels is proposed. The material is regarded as an aggregate of equiaxed crystalline grains containing a random dispersion of pores (large voids due to large irradiation levels) and exhibiting elastic isotropy but viscoplastic anisotropy. The overall properties are obtained via a judicious combination of various bounds and estimates for the elastic energy and viscoplastic dissipation of voided crystals and polycrystals. Reference results are generated with full-field numerical simulations for dense and voided polycrystals with periodic microstructures and crystal plasticity laws accounting for the evolution of dislocation and Frank loop densities. These results are calibrated with experimental data available from the literature and are employed to assess the capabilities of the proposed model to describe the evolution of mechanical properties of highly irradiated Solution Annealed 304L steels at 330°C. The agreement between model predictions and simulations is seen to be quite satisfactory over the entire range of porosities and loadings investigated. The expected decrease of overall elastic properties and strength for porosities observed at large irradiation levels is reported. The mathematical simplicity of the proposed model makes it particularly apt for implementation into finite-element codes for structural safety analyses.

Keywords: crystal plasticity, irradiation hardening, void swelling, Fast Fourier Transforms simulations, austenitic stainless steel, micromechanics of porous media

1. Introduction

Many structural components within the vessel of Pressurized Water Reactors (PWR) are made of austenitic stainless steels. These so-called “internals” are found, for instance, in subsystems associated with many safety functions in western-type PWR, such as for core support, reactivity control, core cooling, and instrumentation availability [1]. In French 1300 MWe nuclear power plants operating under normal conditions, internals are subject to temperatures ranging from 286°C to 370°C [1] and to neutron irradiation doses producing up to a hundred displacements per atoms (dpa) over the reactor lifetime [2]. Such operating environments can induce significant changes in the microstructure and microchemistry of the steel that degrade its mechanical properties [3]. However, the operating environment and ensuing degradation of a particular internal depends on its location relative to the core. This has motivated the development of engineering models to assess the influence of prolonged irradiation periods on the mechanical properties of internals as a function of environmental conditions.

*Corresponding author:

Email address: pierre-guy.vincent@irsn.fr (Pierre-Guy Vincent)

Recent models proposed in [4, 5] rely on finite-element descriptions wherein bulk steel is represented as a periodic aggregate of single crystals and the elastoplastic deformations within the crystals are described by constitutive laws that account for the evolution of dislocation and Frank loop densities [6, 7]. These micromechanical models are able to reproduce the increase in macroscopic tensile strength along with the significant reduction of strain hardening typically observed in irradiated steels, and therefore serve to quantify the degradation of mechanical properties due to irradiation. However, a basic assumption of these models is that the crystals are fully dense. Now, some microscopic analyses of internals of PWR have revealed the occasional presence of intragranular voids or cavities that could be associated with incipient swelling [8, 9]. Many observations of macroscopic void swelling in Fast Breeder Reactors (FBR) have also been reported in the open literature [9]. Swelling normally exhibits an incubation period followed by a steady growth rate in the range of 1% per dpa [9]; it is sensitive to several parameters including chemical composition, heat treatment and mechanical processing of the material, irradiation temperature, dpa and dpa rate, and irradiation spectrum. The presence of such intragranular porosity levels is expected to further degrade the mechanical properties. Motivated by these observations, the purpose of this work is to propose a micromechanical model for quantifying the simultaneous influence of irradiation hardening and swelling on the mechanical stiffness and strength of austenitic steels subject to general stress states. The model regards bulk steel as a polycrystalline aggregate of equiaxed grains containing a random dispersion of voids and exhibiting an elasto-viscoplastic microscopic response. The focus is on large irradiation doses whereby the microscopic response no longer evolves with irradiation damage. The macroscopic elasto-viscoplastic response for a given degree of swelling is then obtained via a judicious combination of various bounds and estimates for the elastic energy and viscoplastic dissipation of voided crystals and polycrystals. Reference results are also generated with full-field numerical simulations for dense and voided polycrystals with periodic microstructures and the crystal plasticity laws of [6, 7]. These results are calibrated with experimental data available from the literature and employed to assess the capabilities of the proposed micromechanical model to describe the evolution of mechanical properties of highly irradiated Solution Annealed 304L steels at 330°C. The proposed model provides the elasto-viscoplastic deformation rate in terms of the stress, the stress rate, and the degree of swelling, as required by common phenomenological models for irradiated stainless steels [10].

2. Analytical model

2.1. Microstructure

Austenitic stainless steels are regarded as random aggregates of perfectly bonded single crystals, or grains, containing a dispersion of microvoids or pores whose level depends on the irradiation dose. Only large voids due to large irradiation levels are considered in this study. Individual grains are assumed to be of similar size, much smaller than the size of the aggregate and the scale of variation of the applied loads, while the voids are assumed to be much smaller than the grains. Furthermore, the aggregates are assumed to have statistically uniform and ergodic microstructures. For simplicity, the model assumes that aggregates are untextured and porosity dispersion is isotropic. This is motivated by an observation reported in [11] on an irradiated SA304L stainless steel, in which the spatial distribution of the cavities was found to be homogeneous.

2.2. Microscopic response

The local deformation of the grains is assumed to be the additive composition of an elastic part and a viscoplastic part due to slip along the standard twelve slip systems of face-centered cubic crystals ($\{111\}\langle 110 \rangle$). The total strain rate is thus written as

$$\dot{\boldsymbol{\epsilon}} = \dot{\boldsymbol{\epsilon}}^{el} + \sum_{s=1}^{12} \dot{\gamma}^{(s)} \boldsymbol{\mu}^{(s)} \quad (1)$$

56 with each term characterized by

$$\dot{\boldsymbol{\varepsilon}}^{el} = \mathbb{S} : \dot{\boldsymbol{\sigma}} \quad \text{and} \quad \dot{\gamma}^{(s)} = \dot{\gamma}_0 \left| \frac{\boldsymbol{\sigma} : \boldsymbol{\mu}^{(s)}}{\tau_0} \right|^n \text{sign} \left(\boldsymbol{\sigma} : \boldsymbol{\mu}^{(s)} \right), \quad (2)$$

57 where $\boldsymbol{\sigma}$, $\boldsymbol{\varepsilon}$, $\boldsymbol{\varepsilon}^{el}$, and $\boldsymbol{\mu}^{(s)}$ denote the local stress, total infinitesimal strain, elastic strain, and Schmid
58 tensors, respectively, $\dot{\gamma}^{(s)}$ denotes the slip rate along the system s , and a dot over a variable denotes its time
59 derivative. The inner product $\boldsymbol{\sigma} : \boldsymbol{\mu}^{(s)}$ of the two second-order tensors $\boldsymbol{\sigma}$ and $\boldsymbol{\mu}^{(s)}$ is defined as $\sigma_{ij} \mu_{ij}^{(s)}$. The
60 Schmid tensor $\boldsymbol{\mu}^{(s)}$ is obtained from the symmetrized dyadic product of the two unit vectors $\mathbf{n}^{(s)}$, normal
61 to the slip plane, and $\mathbf{m}^{(s)}$, along the slip direction of the s^{th} system. They are specified in Appendix A
62 for face-centered cubic crystals. The elastic compliance tensor is taken of the form

$$\mathbb{S} = \frac{1}{3k} \mathbb{J} + \frac{1}{2\mu} \mathbb{K}, \quad (3)$$

63 where \mathbb{J} and \mathbb{K} denote the standard fourth-order isotropic projection tensors [12]. The microscopic response
64 is therefore fully characterized by the bulk and shear moduli k and μ , the creep exponent n , the flow stress
65 τ_0 , and the reference strain rate $\dot{\gamma}_0$. Thus, the description neglects elastic anisotropy, plastic hardening,
66 and variability of flow stress amongst slip systems, allowing for analytical treatment. These simplifications
67 are introduced in order to get an analytical model together with few parameters to be identified. The
68 comparisons provided in Section 4 suggest that this simplified description of the local deformation does not
69 compromise the capabilities of the model.

70 2.3. Macroscopic response

71 The macroscopic response is characterized by the relation between the macroscopic stress $\boldsymbol{\Sigma}$ and strain \boldsymbol{E}
72 tensors, which are identified with the volume averages of their local counterparts over a representative volume
73 element of the voided polycrystal. The proposed model neglects any elastoplastic coupling at this level, so
74 that the macroscopic strain rate $\dot{\boldsymbol{E}}$ is the additive composition of an elastic part $\dot{\boldsymbol{E}}^{el}$ and a viscoplastic part
75 $\dot{\boldsymbol{E}}^{vp}$:

$$\dot{\boldsymbol{E}} = \dot{\boldsymbol{E}}^{el} + \dot{\boldsymbol{E}}^{vp}. \quad (4)$$

76 The dependence of each term on the macroscopic stress tensor $\boldsymbol{\Sigma}$ is obtained by a judicious combination
77 of various bounds and estimates for the elastic energy and viscoplastic dissipation of voided crystals and
78 polycrystals. Mathematical derivations and definitions of the model are provided in Appendix A. The
79 resulting constitutive relations are

$$\dot{\boldsymbol{E}}^{el} = \tilde{\mathbb{S}} : \dot{\boldsymbol{\Sigma}} \quad \text{and} \quad \dot{\boldsymbol{E}}^{vp} = \dot{\gamma}_0 \left| \frac{\lambda}{\tau_0} \right|^n \frac{\frac{f^*}{3} \left(1 - \frac{n-1}{n+1} h^{-2} (\Sigma_m/\lambda) \right) h' (\Sigma_m/\lambda) \mathbf{i} + \frac{3}{\beta} (\Sigma_d/\lambda)}{f^* \left(1 - \frac{n-1}{n+1} h^{-2} (\Sigma_m/\lambda) \right) h' (\Sigma_m/\lambda) (\Sigma_m/\lambda) + \frac{2}{\beta} (\Sigma_{eq}/\lambda)^2} \text{sign}(\lambda), \quad (5)$$

where \mathbf{i} and $\boldsymbol{\Sigma}_d$ denote the identity and stress deviator tensors, respectively, $\Sigma_m = \text{tr}\boldsymbol{\Sigma}/3$ and $\Sigma_{eq} =$
 $\sqrt{(3/2)\boldsymbol{\Sigma}_d : \boldsymbol{\Sigma}_d}$ are the macroscopic hydrostatic and von Mises equivalent stresses, f is the total porosity of
the aggregate for the irradiation level considered—henceforth simply referred to as porosity—, $f^* = qf$ is
a modified porosity by a fixed parameter q , the overall compliance tensor is given by

$$\tilde{\mathbb{S}} = \frac{1}{3\tilde{k}} \mathbb{J} + \frac{1}{2\tilde{\mu}} \mathbb{K} \quad (6)$$

with

$$\tilde{k} = k - f \frac{k}{1 - (1-f) \frac{k}{k+k^*}}, \quad \tilde{\mu} = \mu - f \frac{\mu}{1 - (1-f) \frac{\mu}{\mu+\mu^*}}, \quad k^* = \frac{4}{3}\mu, \quad \mu^* = \frac{\mu}{6} \frac{9k+8\mu}{k+2\mu}, \quad (7)$$

n	1	2	3	5	10	15
α	0.651	1.165	1.397	1.597	1.743	1.789
β	1.502	2.732	3.586	4.541	5.457	5.793

Table 1: Values of α and β entering the gauge surface (8) for some values of exponent n .

Porosity (f)	Number of voids	Mean number of voids per grain	Approximate number of voxels per void
0	0	0	—
0.02	2048	4	1310
0.04	4096	8	1310
0.06	6144	12	1310
0.08	8192	16	1310

Table 2: Description of the microstructures.

80 the gauge factor λ is solution to the nonlinear equation

$$\frac{1}{\beta}(\Sigma_{eq}/\lambda)^2 + f^* \left(h(\Sigma_m/\lambda) + \frac{n-1}{n+1} h^{-1}(\Sigma_m/\lambda) \right) = 1 + \frac{n-1}{n+1} f^{*2}, \quad (8)$$

81 and the function h , with derivative h' , is given by

$$h(x) = \left(1 + \frac{|x|^{1+\frac{1}{n}}}{\alpha n} \right)^n. \quad (9)$$

82 The coefficients α and β in these expressions depend on the creep exponent n and local plastic anisotropy
83 as discussed in Appendix A. Table 1 specifies numerical values for common creep exponents and the local
84 plastic anisotropy assumed by (1)-(2) for face-centered cubic crystals. This set of expressions serves to fully
85 characterize the elasto-viscoplastic response of the porous polycrystalline aggregate for any multiaxial loading
86 history. As irradiation dose progresses, the porosity f —and eventually some local material parameters—
87 will evolve. The resulting stiffness is dictated by expressions (7) —the Young’s modulus following from
88 $\tilde{E} = 9\tilde{k}\tilde{\mu}/(\tilde{\mu} + 3\tilde{k})$ —, while the resulting strength is identified with the flow stress deep in the plastic range.

89 3. Numerical model

90 3.1. Microstructure

91 In contrast to the analytical model considered above, the numerical model idealizes stainless steels as
92 periodic aggregates of grains describing a Voronoi tessellation and containing an isotropic distribution of
93 spherical voids. Figure 1 shows the various unit cells employed in this study. These cells contain 512 grains
94 and a varying number of intragranular mono-sized voids. The same Voronoi tessellation is used for all these
95 microstructures. For porosity levels of 0.02 or 0.04, three distinct sets of positions of the centers of the voids
96 are considered. For each of these microstructures, the porosity over the whole volume and the number of
97 voids in the total volume is prescribed. It is noted that the voids are always of the same size, and are located
98 entirely inside the grains, even though numerous voids may fall in areas close to the grain boundaries. The
99 centers of the voids are supposed to be randomly distributed inside the grains. The precise number of
100 grains and voids employed follows from the parametric study reported in Appendix B. A summary of these
101 microstructural parameters is provided in Table 2.

102 3.2. Microscopic response

103 The local deformation of the grains is assumed to follow a physically-based crystal plasticity law recently
104 developed by [6, 7] specifically for irradiated SA304L steels at 330°C. This crystal plasticity law was used

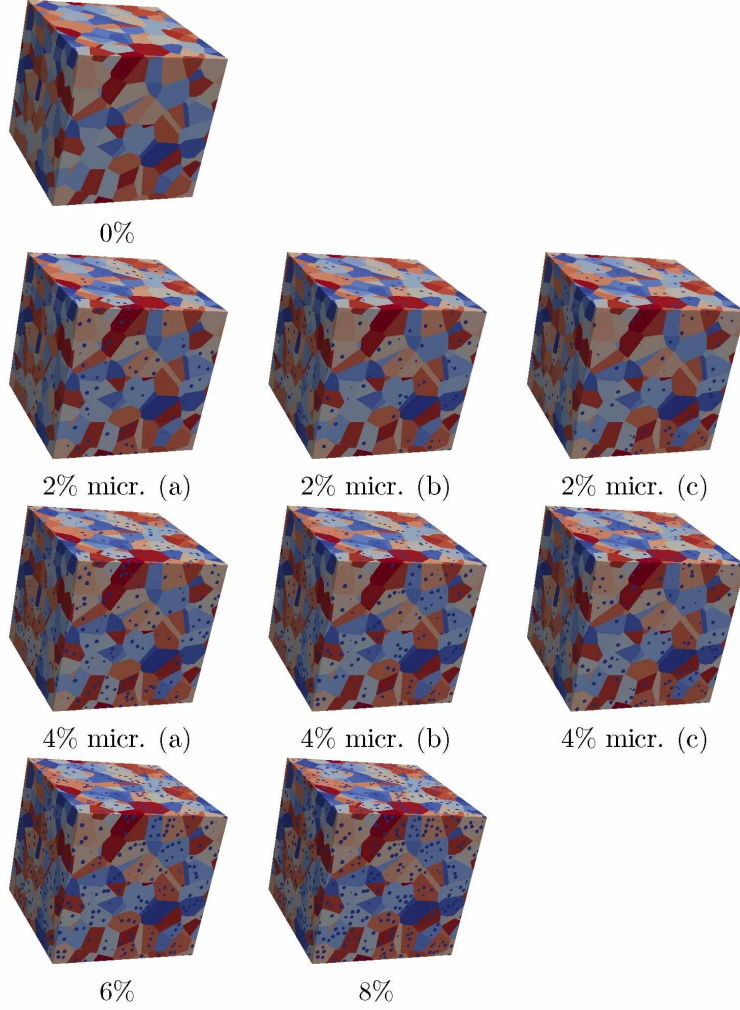


Figure 1: Microstructures employed in numerical model for various porosity levels and number of voids. Three different void distributions are considered in microstructures with porosity levels 2% and 4%.

105 by [4] for studying the intergranular stress distribution in irradiated stainless steels, by [13] for studying
 106 the void growth and coalescence of voids in irradiated face-centered cubic single crystals, and by [14] for
 107 a comparison between finite element and Fast Fourier transforms-based methods simulations. This law
 108 assumes the same additive form (1)-(2) for the local deformation but with the slip rates given by

$$\dot{\gamma}^{(s)} = \left\{ \frac{|\boldsymbol{\sigma} : \boldsymbol{\mu}^{(s)}| - \tau_c^{(s)}}{K_0} \right\}^n \text{sign}(\boldsymbol{\sigma} : \boldsymbol{\mu}^{(s)}), \quad (10)$$

109 where K_0 is a Norton parameter and $\{\cdot\}$ denote the Macaulay brackets. In turn, the material parameters
 110 $\tau_c^{(s)}$ represent critical resolved shear stresses that evolve with plastic deformation according to a hardening
 111 law of the form

$$\tau_c^{(s)} = \bar{\tau}_0 + \tau_a \exp\left(-\frac{|\dot{\gamma}^{(s)}|}{\bar{\gamma}_0}\right) + \bar{\mu} \sqrt{\sum_{u=1}^{12} a_{su} r_D^{(u)}} + \alpha_L \bar{\mu} \sqrt{\sum_{p=1}^4 r_L^{(p)}}, \quad (11)$$

112 where the internal variables $r_D^{(s)}$ and $r_L^{(p)}$ represent, respectively, normalized densities of dislocations moving
 113 along the twelve crystallographic directions $\{111\}\langle 110 \rangle$ and densities of Frank loops defined on the four

114 crystallographic planes $\{111\}$, which in turn evolve with plastic deformation according to

$$\dot{r}_D^{(s)} = \left(\frac{1}{\bar{\kappa}} \sqrt{\sum_{u=1}^{12} b_{su} r_D^{(u)}} + \frac{1}{\bar{\kappa}} \sqrt{K_{dl} \sum_{p=1}^4 r_L^{(p)} - G_c r_D^{(s)}} \right) |\dot{\gamma}^{(s)}| \quad (12)$$

115 and

$$\dot{r}_L^{(p)} = -A_L (r_L^{(p)} - r_L^{sat}) \left(\sum_{s \in \text{plane } p}^3 |\dot{\gamma}^{(s)}| \right) \left(\sum_{s \in \text{plane } p}^3 r_D^{(s)} \right). \quad (13)$$

116 Unlike the law employed in the analytical model, this law accounts for elastic anisotropy and plastic
 117 hardening. Elastic anisotropy is accounted for by assuming a cubic elasticity tensor $\mathbb{C} \equiv \mathbb{S}^{-1}$; plastic
 118 hardening is accounted for via twelve dislocation densities and four Frank loop densities. The critical
 119 resolved stresses are coupled with the dislocation densities via a twelve by twelve dislocation interaction
 120 matrix a_{su} with six independent parameters (general form specified in Appendix A), while the various
 121 dislocation densities are themselves coupled via a twelve by twelve matrix b_{su} indicated in Table 3. Initially,
 122 the normalized dislocation densities are assumed to take the same value r_D^0 in all slip systems, and the
 123 normalized Frank loop densities are assumed to take the same value r_L^0 for all slip planes. To account for
 124 a dislocation unlock mechanism, a reference slip denoted by $\bar{\gamma}_0$ has been introduced to adjust the speed
 125 of avalanche after unlocking the dislocations. For a detailed description of the physical basis behind this
 126 description the reader is referred to [6, 7, 4].

127 3.3. Macroscopic response

128 As in the analytical model, the macroscopic response is identified with the relation between the volume
 129 averages of the stress and strain fields over a representative volume element. To compute these fields for given
 130 loading conditions, the above constitutive equations were implemented in the software CraFT [15] which
 131 solves the mechanical field equations by means of a Fast-Fourier Transform (FFT) algorithm proposed by
 132 [16] and [17] to determine the effective properties of periodic composites, and integrates the response in
 133 time with a fully implicit scheme [18]. Following the work of [19] on porous viscoplastic crystals, we adopt
 134 the FFT algorithm often referred to as the “basic scheme” which ensures strain compatibility. The scheme
 135 discretizes the unit cell with a regular grid composed of voxels. Based on the parametric study reported in
 136 Appendix B we adopt a grid of 512^3 voxels so that there are 64^3 voxels per grain on average and about
 137 1310 voxels per void.

138 Results are generated by imposing mixed loading conditions [20]: the direction of the overall stress (Σ^o)
 139 is prescribed together with the strain-rate in this direction. At each iteration j of the general algorithm,
 140 two errors are computed to check convergence. One is relative to the local equilibrium condition,

$$\text{err}_1(j) = \frac{\left\langle \|\text{div } \boldsymbol{\sigma}^{(j)}\|^2 \right\rangle^{1/2}}{\|\langle \boldsymbol{\sigma}^{(j)} \rangle\|}, \quad (14)$$

141 while the other is relative to the prescribed direction of the macroscopic stress:

$$\text{err}_2(j) = \frac{\|\langle \boldsymbol{\sigma}^{(j)} \rangle - \bar{\kappa} \Sigma^o\|}{\|\bar{\kappa} \Sigma^o\|}. \quad (15)$$

142 Here, $\bar{\kappa}$ indicates the unknown level of overall stress, $\langle \boldsymbol{\sigma}^{(j)} \rangle$ is the volume average of the stress at iteration j
 143 (with the following notation $\langle \cdot \rangle = 1/|\Omega| \int_{\Omega} \cdot d\Omega$, where Ω is the entire domain) and $\|\cdot\|$ denotes the Euclidean
 144 norm squared. The iterative procedure is stopped when the errors err_1 and err_2 are respectively smaller
 145 than 10^{-2} and 10^{-4} .

146 In the sequel, predictions for a tensile loading are obtained by fixing a macroscopic stress direction with
 147 only one non-vanishing component $\Sigma_{33} > 0$, applying a strain rate $\dot{E}_{33} = 3 \times 10^{-4} \text{ s}^{-1}$, and stopping when

\mathbf{C}_{11}		\mathbf{C}_{12}		\mathbf{C}_{44}		$\bar{\mu}$	K_0		τ_a
199 GPa		136 GPa		105 GPa		65.5 GPa	10 MPa s ^{1/n}		61.2 MPa
n	G_c	$\bar{\kappa}$	a_1	a_2	a_3	a_4	a_5	a_6	
15	10.4	42.8	0.124	0.124	0.070	0.625	0.137	0.122	
b_{ii}	$b_{ij} \ i \neq j$	r_D^0	r_L^0	K_{dl}	α_L	A_L	r_L^{sat}		
0	1	1.03 10 ⁻¹¹	4.9 10 ⁻⁶	2.50 10 ⁻⁷	0.57	5.548 10 ⁸	3.234 10 ⁻⁶		

Table 3: Model parameters for SA304L stainless steel at 330°C and irradiated to 13 dpa, taken from [6]. Top row: parameters in absolute units. Middle and bottom row: normalized parameters.

148 E_{33} reaches 3×10^{-2} . In turn, predictions for a purely hydrostatic loading are obtained by fixing Σ^o equal
149 to the identity tensor, applying a hydrostatic strain rate $\dot{E}_m = (\dot{E}_{11} + \dot{E}_{22} + \dot{E}_{33})/3 = 3 \times 10^{-4} \text{ s}^{-1}$, and
150 stopping when E_m reaches 3×10^{-2} . Finally, mixed stress states are obtained by fixing

$$\Sigma^o = \begin{pmatrix} \Sigma_{11}^o & 0 & 0 \\ 0 & \Sigma_{11}^o & 0 \\ 0 & 0 & 1 \end{pmatrix} \quad \text{with} \quad 0 \leq \Sigma_{11}^o \leq 1, \quad (16)$$

151 applying the rate $\Sigma_{11}^o \dot{E}_{11} + \Sigma_{11}^o \dot{E}_{22} + \dot{E}_{33} = 9 \times 10^{-4} \text{ s}^{-1}$, and stopping when that combination reaches
152 9×10^{-2} . Another stress state including simple shear is tested by fixing

$$\Sigma^o = \begin{pmatrix} 1 & \Sigma_{12}^o & 0 \\ \Sigma_{12}^o & 1 & 0 \\ 0 & 0 & 1 \end{pmatrix} \quad \text{with} \quad 0 \leq \Sigma_{12}^o \leq 1.732, \quad (17)$$

153 applying the rate $\dot{E}_{11} + \dot{E}_{22} + \dot{E}_{33} + 2\Sigma_{12}^o \dot{E}_{12} = 9 \times 10^{-4} \text{ s}^{-1}$, and stopping when that combination reaches
154 9×10^{-2} .

155 4. Results

156 4.1. Numerical model versus experimental observations

157 We begin by calibrating the numerical model of Section 3 with available experimental observations for
158 fully dense steels. To that end, we adopt all material parameters from reference [6] with the exception
159 of $\bar{\gamma}_0$ and $\bar{\tau}_0$. The various numerical values are given in Table 3 with the elastic constants reported in
160 Voigt notation. A relatively high creep exponent is employed to represent a low strain-rate sensitivity. The
161 remaining parameters $\bar{\gamma}_0$ and $\bar{\tau}_0$ are then used to fit various tensile curves of irradiated SA304L steels at
162 about 300°C and high exposure levels—at least 10 dpa—reported by [6, 4, 21]. Figure 2 shows comparisons
163 between those measurements and numerical predictions obtained with $\bar{\gamma}_0 = 0.5$ and $\bar{\tau}_0 = 58 \text{ MPa}$. These
164 values are seen to reproduce the experimental measurements with reasonable accuracy. In this connection,
165 it is observed that the experimental curves exhibit a slight softening just after the maximal stress. In line
166 with [6], we understand that this softening is not due to the stretching of the tensile specimen or to the
167 ductile damage, but rather due to the specific dislocation dynamics. The crystal plasticity laws of Section
168 3.2 can reproduce such a peak with a suitable choice of parameters. Indeed, $\bar{\gamma}_0$ adjusts the speed of avalanche
169 after unlocking the dislocations, and therefore decreasing its value enhances the peak on the overall stress-
170 strain curve of the polycrystal—often called “yield point” phenomenon—, while $\bar{\tau}_0$ adjusts the maximum
171 stress level. However, numerical results for material responses with well-defined peaks were found to exhibit
172 pronounced dependences on the grid size. For this reason, we have opted for a description that identifies
173 maximum stress levels with those developed deep in the plastic range.

174 The calibrated model is now used to generate results for porous materials. Figure 3 shows the tensile
175 curves obtained with the various microstructures presented in Section 3. As expected, intragranular porosity

176 reduces the overall Young's modulus and the maximal overall stress. It is seen that the three microstructures
 177 with 2% porosity —microstructures (a), (b) and (c) in Figure 1— lead to similar tensile curves: the full-line,
 178 dashed and dotted curves in Figure 3 are visually indistinguishable. A similar conclusion is reached for
 179 4% porosity. This confirms the appropriate representativeness of the distribution voids within the unit cell.
 180 Thus, we can extract from these curves representative results for the evolution of Young's modulus and
 181 maximal stress with swelling, and compare them with experimental measurements.

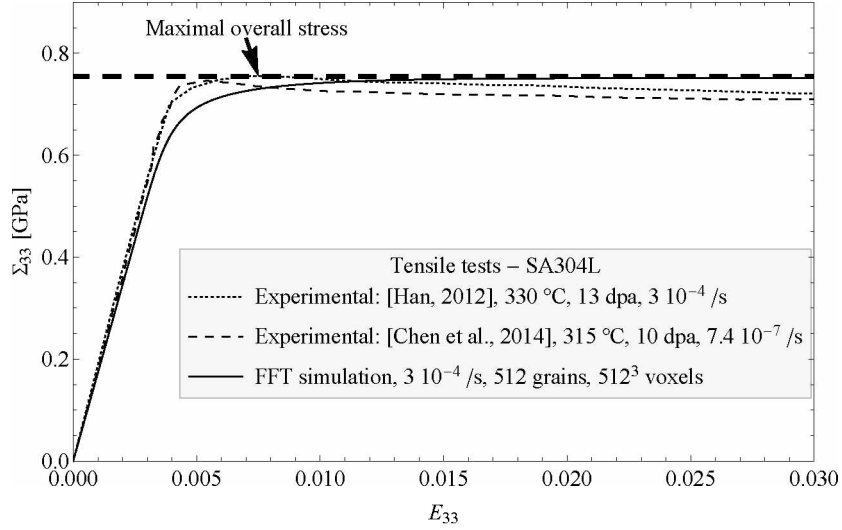


Figure 2: Tensile response. Comparison between experiments and numerical model.

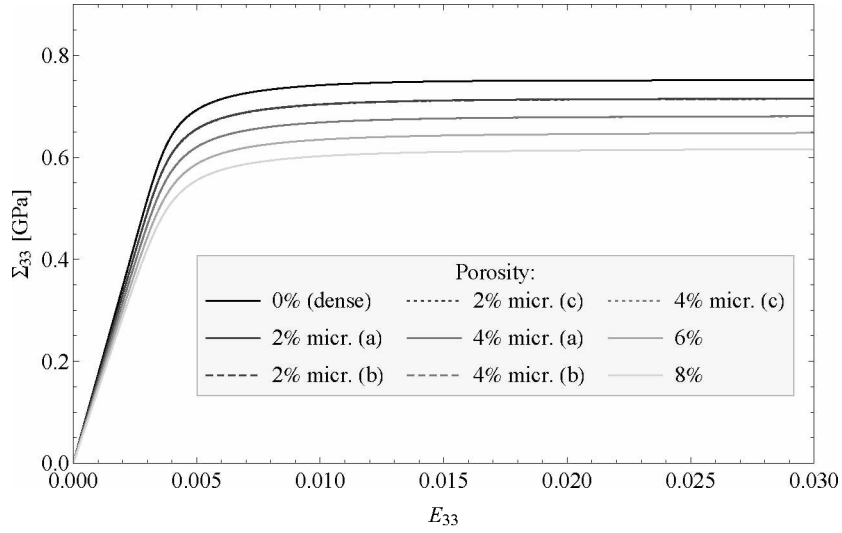


Figure 3: Numerical predictions for the tensile response of porous polycrystals with the microstructures of Figure 1.

182 The evolution of the overall Young's modulus \tilde{E} as a function of swelling is reported in Figure 4, along
 183 with experimental measurements of [22] and [23] on a Russian cold-worked austenitic steel. Here, the swelling
 184 is defined in terms of the porosity f as $f/(1-f)$, and \tilde{E}_0 denotes the Young's modulus for the fully dense
 185 material. The tested samples were cut from fuel element cladding tubes that had been irradiated in the
 186 BN-600 fast reactor. The numerical model is found to be in reasonable accord with experiments. According
 187 to the model, a porosity level of 8% causes a 15% reduction in Young's modulus.

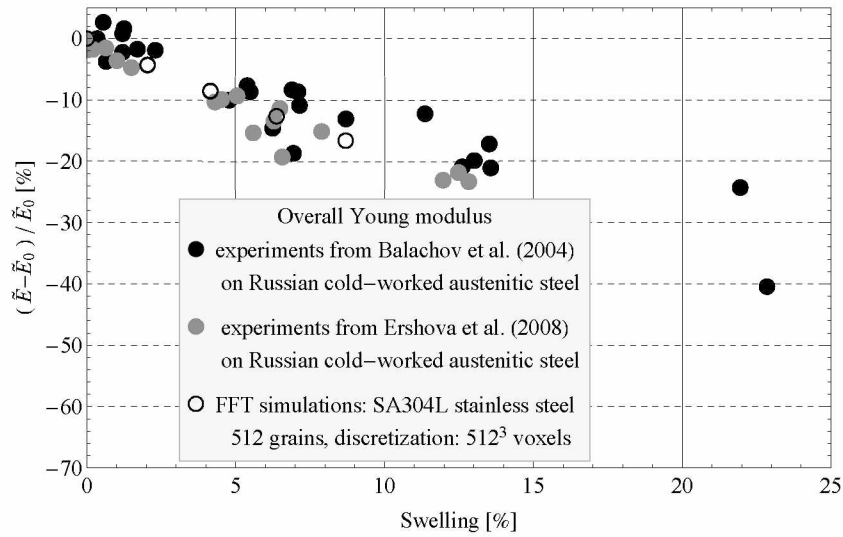


Figure 4: Overall Young's modulus as a function of swelling.

188 The corresponding evolution of overall maximal stress \tilde{R}_m in simulations and experiments is reported in
 189 Figure 5, along with experimental measurements of [24] on a Russian Kh18H10T annealed austenitic stainless
 190 steel. The tested samples come from a duct irradiated in the BOR-60 fast reactor. In this connection, it is
 191 recalled that the Kh18H10T steel is the primary construction material of internals in Russian water-cooled,
 192 water-moderated energy reactors, and that the closest Western analog of this material is the 321 stainless
 193 steel [24]. Results reported in Figure 5 correspond to tests conducted at or near the irradiation temperature,
 194 from 360°C to 430°C. Once again, the numerical model is found to be in reasonable accord with experiments.
 195 According to the model, a porosity level of 8% causes a 20% reduction in maximal stress.

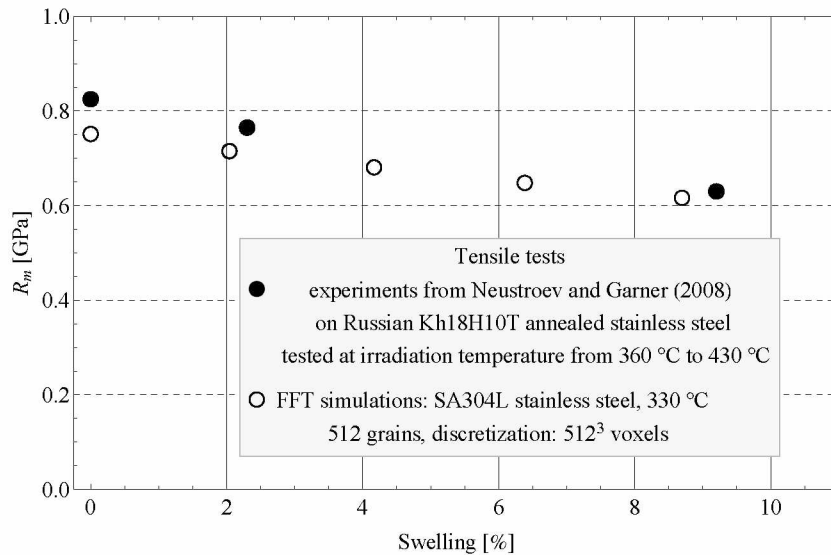


Figure 5: Overall maximal stress as a function of swelling.

k	μ	n	$\dot{\gamma}_0$	τ_0	α	β	q
156.7 GPa	65.7 GPa	15	1 s ⁻¹	498 MPa	1.789	5.793	2

Table 4: Parameters of the analytical model.

196 4.2. Analytical versus numerical models

197 The above numerical model is now used to assess the capabilities of the simple analytical model presented
198 in Section 2.3 to reproduce the response of a SA304L at 330°C. We begin by calibrating the analytical model
199 with the tensile response of a fully dense material predicted by the numerical model. To that end, analytical
200 predictions are obtained by integrating in time equations (4) and (5) using an explicit Runge-Kutta 3(2)
201 method with adaptative time step. At each iteration, the value of $|\lambda|$ is obtained by solving the non-linear
202 equation (8) with a Newton method. Following [6], the local elastic moduli are set to $k = 156.7$ GPa and
203 $\mu = 65.7$ GPa. In turn, the creep exponent n is set to the same value as in the numerical model, i.e. $n = 15$,
204 and the reference strain-rate is set to $\dot{\gamma}_0 = 1$ s⁻¹. For that creep exponent, the coefficients α and β are given
205 by 1.789 and 5.793, respectively. Finally, a suitable value for the flow stress τ_0 is identified by confronting
206 the analytical and numerical responses. The comparison shown in Figure 6 corresponds to $\tau_0 = 498$ MPa,
207 which is deemed suitable. The complete set of material parameters is summerized in Table 4.

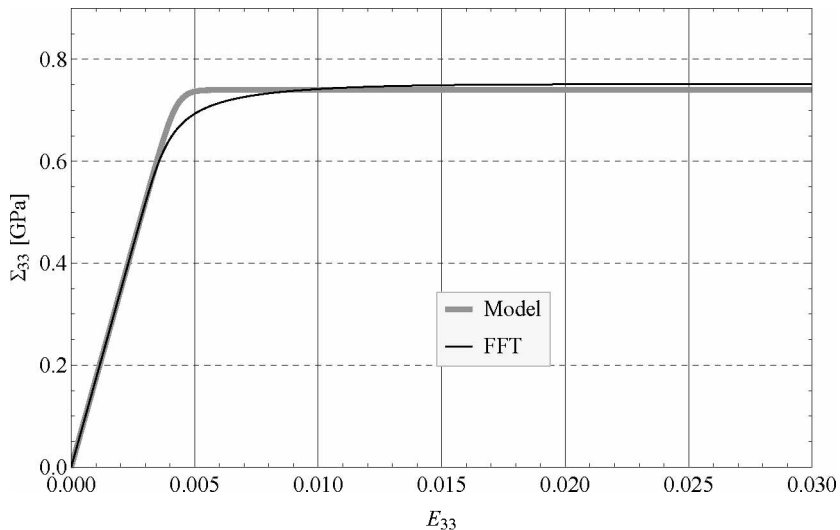


Figure 6: Tensile curves: comparison between analytical and numerical predictions for the choice $\tau_0 = 498$ MPa.

208 Having calibrated the analytical model with the response for fully dense materials, we can confront the
209 analytical and numerical predictions for porous materials. Figures 8 and 9 show comparisons for the overall
210 Young’s modulus and bulk modulus versus porosity. It is recalled that, in view of the overall isotropy, these
211 two parameters completely characterize the elastic response. The agreement between the models is seen to
212 be quite satisfactory over the entire range of porosity levels considered. This is in line with the observations
213 of [25] and theoretical predictions of [26]. Note that the numerical predictions for the bulk modulus are
214 obtained from the purely hydrostatic loading case presented in 3.3 and reported in Figure 7.

215 The analytical description of the viscoplastic response contains an additional parameter q in the definition
216 of the modified porosity f^* . This parameter has been introduced following the experience of [27] with the
217 so-called standard GTN model for isotropic porous plasticity to adjust the porosity percolation threshold
218 at which the material is expected to completely loose its load carrying capacity [28]. A suitable value for
219 q is identified by comparing the analytical and numerical predictions for the overall maximal stress under
220 uniaxial tension. Figure 10 shows a comparison for $q = 2$. Based on the good agreement observed, this value
221 is deemed suitable. In this connection, it should be noted that the analytical model does not account for

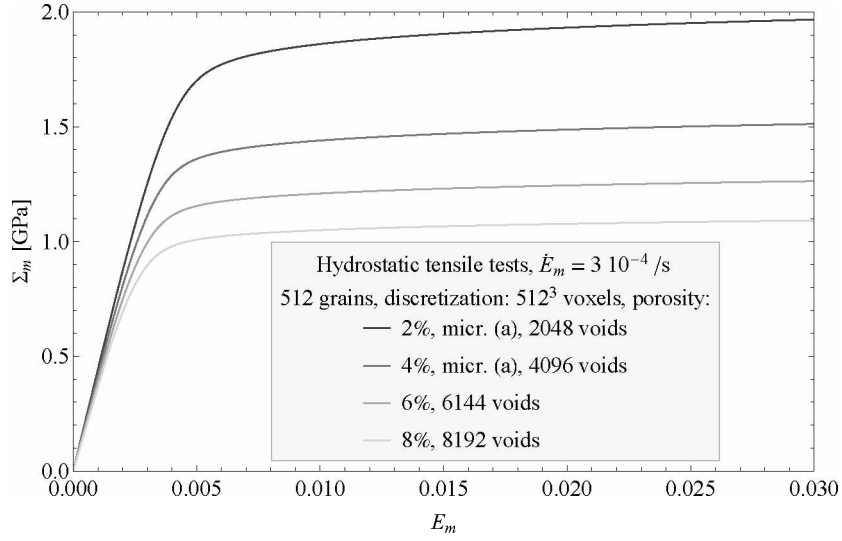


Figure 7: Porous polycrystals under purely hydrostatic loading. Numerical simulations performed on the microstructures of Figure 1.

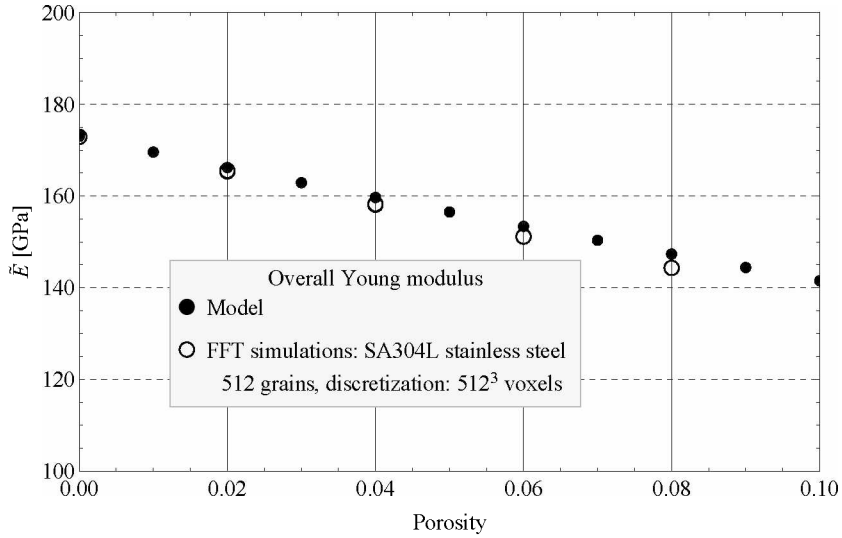


Figure 8: Evolution of the overall Young modulus with respect to the porosity: micromechanical model and FFT-based numerical full-field simulations.

222 plastic softening and therefore does not exhibit a rigorous maximal stress. The maximal stress reported in
 223 this figure corresponds to the stress level deep in the plastic range. Given the large creep exponent employed,
 224 this stress level is relatively insensitive to the strain rate, at least within the range of strain rates of interested
 225 in applications. Having fixed this last parameter, no further fitting is required. The analytical model now
 226 provides a predictive tool for the material response under general loading conditions. Figure 11 shows a
 227 comparison between the analytical and numerical estimates for the overall maximal stress under hydrostatic
 228 tension. Analytical predictions are seen to remain accurate for this loading condition in the entire range
 229 of porosity levels considered. To confirm the accuracy of the model for more general loading conditions,
 230 further comparisons are reported for the multiaxial stress states defined in Section 3.3. The macroscopic
 231 hydrostatic and equivalent stresses obtained at the end of the simulations of a specimen with moderate

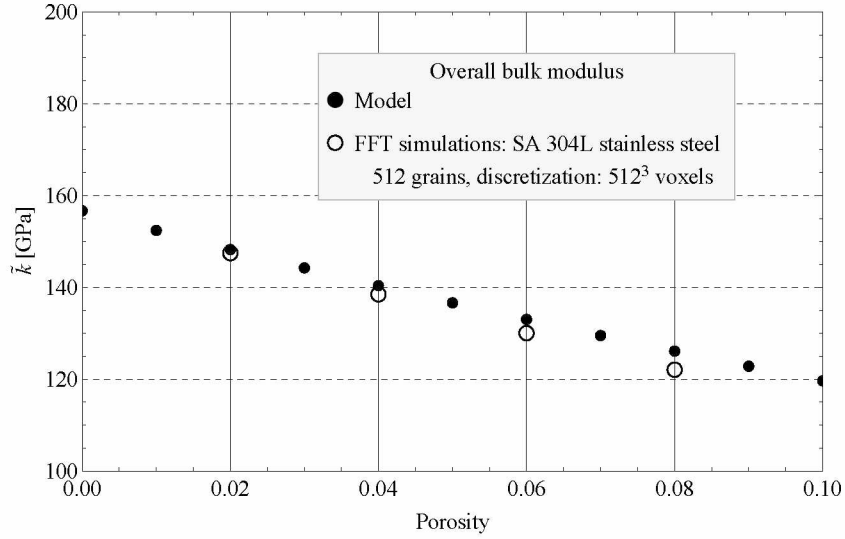


Figure 9: Evolution of the overall bulk modulus with respect to the porosity: micromechanical model and FFT-based numerical full-field simulations.

232 porosity level are plotted in Figures 12 and 13. Once again, the agreement is seen to be satisfactory over the
 233 whole range of stress states investigated despite the fact that some of these stress states induce a different
 234 plastic anisotropy from that induced by the uniaxial loading employed in the calibration of the model.

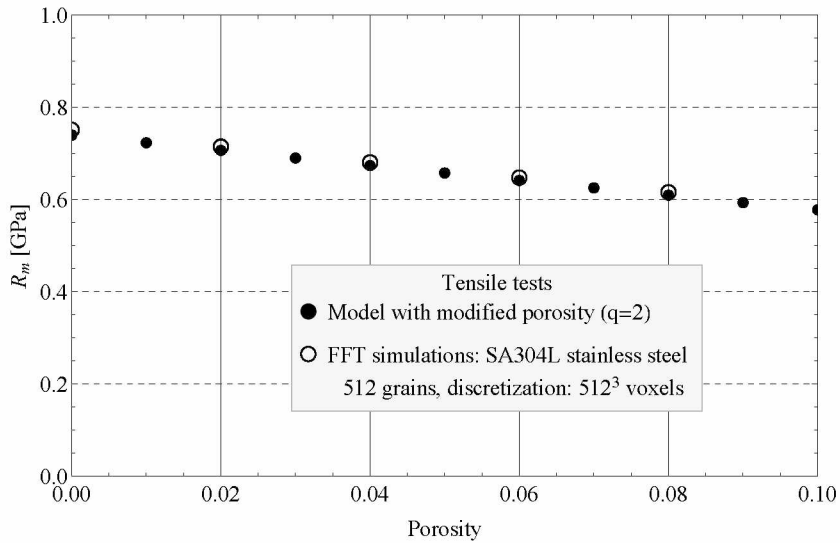


Figure 10: Overall maximal stress under uniaxial tension versus porosity: comparison between analytical and numerical models.

235 5. Conclusions

236 A micromechanical model for quantifying the simultaneous influence of irradiation hardening and swelling
 237 on the mechanical stiffness and strength of neutron-irradiated austenitic stainless steels has been proposed.
 238 The model makes use of several simplifying assumptions allowing for a fully explicit elasto-viscoplastic
 239 description. In turn, reference results were generated with full-field numerical simulations for dense and

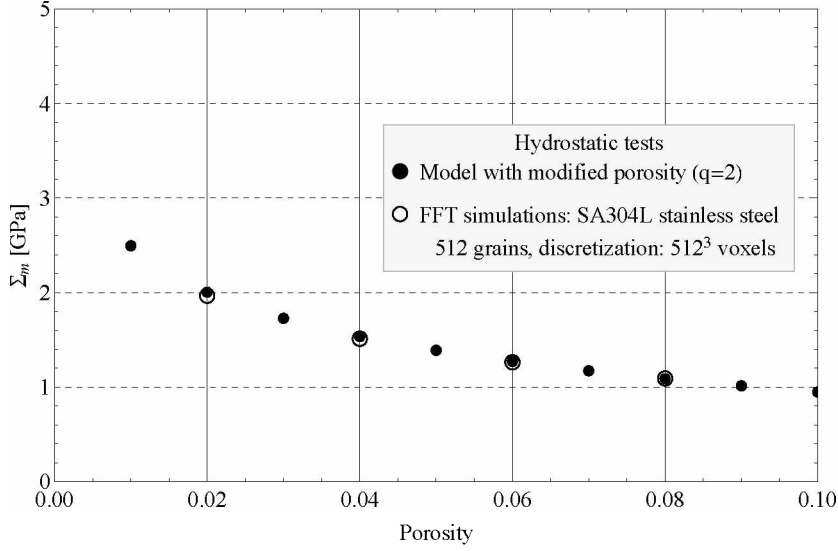


Figure 11: Overall maximal stress under hydrostatic tension versus porosity: comparison between the analytical and numerical models.

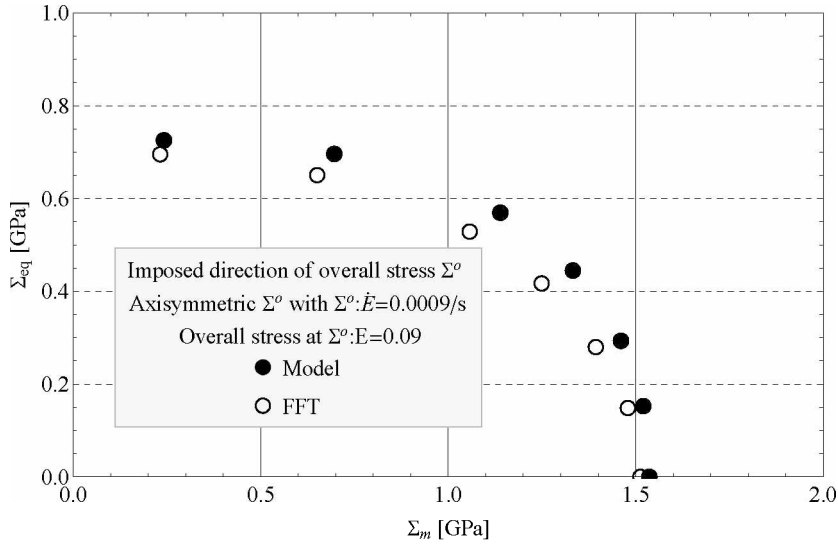


Figure 12: Axisymmetric direction of macroscopic stress Σ° as specified in (16). Macroscopic hydrostatic and equivalent stresses obtained at the end of the simulations. Comparison between the micromechanical model and the FFT simulations. FFT simulations performed on the microstructure (a) with 4% porosity of Figure 1.

240 voided polycrystals with periodic microstructures and crystal plasticity laws accounting for the evolution of
 241 dislocation and Frank loop densities. These results were calibrated with experimental data available from
 242 the literature and were employed to assess the capabilities of the proposed model to describe the evolution of
 243 mechanical properties of highly irradiated Solution Annealed 304L steels at 330°C. The agreement between
 244 analytical and numerical predictions for stiffness and mechanical strength was found to be quite satisfactory
 245 over the entire range of porosities and loadings investigated. The expected decrease of these properties for
 246 porosities observed at large irradiation levels has been reported for porosity levels up to 8%. The simplicity
 247 of the analytical model comes at the expense of neglecting the influence of local elastic anisotropy and
 248 plastic hardening on the overall response. While the former is indeed negligible, the latter may be non-

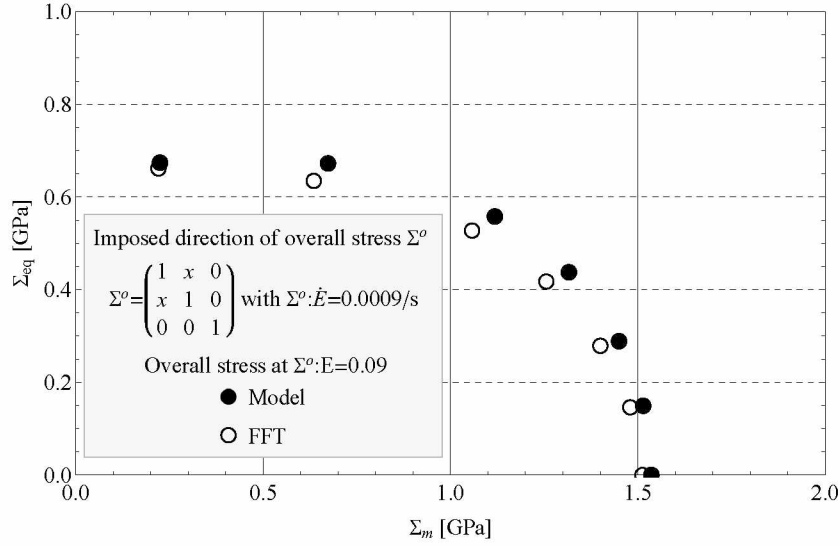


Figure 13: Direction of macroscopic stress Σ^o including simple shear as specified in (17). Macroscopic hydrostatic and equivalent stresses obtained at the end of the simulations. Comparison between the micromechanical model and the FFT simulations. FFT simulations performed on the microstructure (a) with 4% porosity of Figure 1.

249 negligible at least for some aspects of the overall response not considered in this work, such as strain to
 250 failure. Fortunately, the multiscale nature of the analytical model could be exploited to incorporate plastic
 251 hardening through appropriate evolution laws for the local flow stress. In terms of the mechanical properties
 252 considered in this work, however, the analytical model seems suitable. Furthermore, in view of its capabilities
 253 and mathematical simplicity, the model is considered particularly apt for implementation into finite-element
 254 codes for structural safety analyses.

255 Acknowledgments

256 H.M. and P-G.V. acknowledge the financial support from European Committee through the SOTERIA
 257 H2020 research project funded under the Euratom research and training programme 2014-2018 under grant
 258 agreement N° 661913. Some of the full-field simulations presented here were made possible thanks to the
 259 resources of the CCRT (Centre de Calcul Recherche et Technologie) of the CEA/DIF.

260 Data availability

261 The raw and processed data required to reproduce these findings are available from the corresponding
 262 author upon reasonable request.

263 References

- 264 [1] INTERNATIONAL ATOMIC ENERGY AGENCY, Assessment and Management of Ageing of Major Nuclear Power Plant
 265 Components Important to Safety: PWR Vessel Internals, INTERNATIONAL ATOMIC ENERGY AGENCY, Vienna,
 266 1999, IAEA-TECDOC-1119.
 267 [2] F. Garner, L. Greenwood, D. Harrod, Potential high fluence response of pressure vessel internals constructed from austenitic
 268 stainless steels, in: 6th International Symposium on Environmental Degradation of Materials in Nuclear Power Systems-
 269 Water Reactors, 1993, pp. 783–790.
 270 [3] O. Chopra, A. Rao, A review of irradiation effects on LWR core internal materials neutron embrittlement, Journal of
 271 Nuclear Materials 412 (1) (2011) 195 – 208.
 272 [4] J. Hure, S. E. Shawish, L. Cizelj, B. Tanguy, Intergranular stress distributions in polycrystalline aggregates of irradiated
 273 stainless steel, Journal of Nuclear Materials 476 (2016) 231 – 242.

- 274 [5] S. E. Shawish, J. Hure, Intergranular normal stress distributions in untextured polycrystalline aggregates, *European*
275 *Journal of Mechanics - A/Solids* 72 (2018) 354 – 373.
- 276 [6] X. Han, Modélisation de la fragilisation due au gonflement dans les aciers inoxydables austénitiques irradiés, Ph.D. thesis,
277 Ecole Nationale Supérieure des Mines de Paris (2012).
- 278 [7] B. Tanguy, X. Han, J. Besson, S. Forest, C. Robertson, N. Rupin, Dislocations and irradiation defects-based microme-
279 chanical modelling for neutron irradiated austenitic stainless steels, in: *International Symposium on Plasticity 2013 and*
280 *Its Current Applications*, 2013.
- 281 [8] F. A. Garner, D. J. Edwards, S. M. Bruemmer, S. I. Porollo, Y. V. Konobeev, V. S. Neustroev, V. K. Shamardin,
282 A. V. Kozlov, I. I. Balachov, Y. Isobe, Recent developments concerning void swelling in PWR internals at relatively
283 low irradiation temperatures, in: *The Fifth International Ural Seminar on the Radiation Physics of Metals and Alloys:*
284 *Abstracts of Papers*, 2003, p. 133, February 1 March 1, 2003, Snezhinsk.
- 285 [9] F. Garner, 4.02 - radiation damage in austenitic steels, in: R. J. Konings (Ed.), *Comprehensive Nuclear Materials*, Elsevier,
286 Oxford, 2012, pp. 33 – 95.
- 287 [10] J.-L. Fléjou, Comportement élasto-plastique sous irradiation des métaux : application aux internes de cuve, in: *Manuel*
288 *de référence. Code_Aster*, 2010, 4284.
- 289 [11] A. Renault, J. Malaplate, C. Pokor, P. Gavoille, TEM and EFTEM characterization of solution annealed 304L stainless
290 steel irradiated in PHENIX, up to 36dpa and at 390C, *Journal of Nuclear Materials* 421 (1) (2012) 124 – 131.
- 291 [12] P. Suquet, M. Bornert, Rappels de calcul tensoriel et d'élasticité, in: M. Bornert, T. Bretheau, P. Gilormini (Eds.),
292 *Homogénéisation en mécanique des matériaux*, Vol. 2, Hermès Science Publications, Paris, 2001, Ch. 5, pp. 171–202.
- 293 [13] C. Ling, B. Tanguy, J. Besson, S. Forest, F. Latourte, Void growth and coalescence in triaxial stress fields in irradiated
294 FCC single crystals, *Journal of Nuclear Materials* 492 (2017) 157 – 170.
- 295 [14] S. E. Shawish, P.-G. Vincent, H. Moulinec, L. Cizelj, L. Gélébart, Full-field polycrystal plasticity simulations of neutron-
296 irradiated austenitic stainless steel: A comparison between FE and FFT-based approaches, *Journal of Nuclear Materials*
297 529 (2020) 151927.
- 298 [15] P. Suquet, H. Moulinec, O. Castelnau, M. Montagnat, N. Lahellec, F. Grennerat, P. Duval, R. Brenner, Multi-scale
299 modeling of the mechanical behavior of polycrystalline ice under transient creep, *Procedia IUTAM* 3 (2012) 76 – 90,
300 IUTAM Symposium on Linking Scales in Computations: From Microstructure to Macro-scale Properties.
- 301 [16] H. Moulinec, P. Suquet, A fast numerical method for computing the linear and nonlinear properties of composites, *C. R.*
302 *Acad. Sc. Paris II* 318 (1994) 1417–1423.
- 303 [17] H. Moulinec, P. Suquet, A numerical method for computing the overall response of nonlinear composites with complex
304 microstructure, *Computer Methods in Applied Mechanics and Engineering* 157 (1998) 69–94.
- 305 [18] L. Joëssel, Micromechanical modeling of the viscoplastic behavior of a porous polycrystal: application to an irradiated
306 austenitic stainless steel, Ph.D. thesis, Université d'Aix-Marseille (2018).
- 307 [19] L. Joëssel, P.-G. Vincent, M. Gäråjeu, M. I. Idiart, Viscoplasticity of voided cubic crystals under hydrostatic loading,
308 *International Journal of Solids and Structures* 147 (2018) 156 – 165.
- 309 [20] J. Michel, H. Moulinec, P. Suquet, Effective properties of composite materials with periodic microstructure: a computa-
310 tional approach, *Computer Methods in Applied Mechanics and Engineering* 172 (1) (1999) 109 – 143.
- 311 [21] Y. Chen, A. Rao, B. Alexandreanu, K. Natesan, Slow strain rate tensile tests on irradiated austenitic stainless steels
312 in simulated light water reactor environments, *Nuclear Engineering and Design* 269 (2014) 38 – 44, special Issue - The
313 *International Conference on Structural Mechanics in Reactor Technology (SMiRT21)*, New Delhi India, Nov 06-11, 2011.
- 314 [22] I. I. Balachov, E. Shcherbakov, A. Kozlov, I. Portnykh, F. Garner, Influence of radiation-induced voids and bubbles on
315 physical properties of austenitic structural alloys, *Journal of Nuclear Materials* 329-333 (2004) 617 – 620, proceedings of
316 the 11th International Conference on Fusion Reactor Materials (ICFRM-11).
- 317 [23] O. V. Ershova, E. N. Shcherbakov, P. I. Yagovitin, M. V. Evseev, V. S. Shikhalev, A. V. Kozlov, Relation between the
318 physicomechanical properties of an austenitic ChS-68 steel and its swelling during high-dose irradiation, *The Physics of*
319 *Metals and Metallography* 106 (6) (2008) 624–629.
- 320 [24] V. Neustroev, F. Garner, Very high swelling and embrittlement observed in a Fe18Cr10NiTi hexagonal fuel wrapper
321 irradiated in the BOR-60 fast reactor, *Journal of Nuclear Materials* 378 (3) (2008) 327 – 332.
- 322 [25] E. A. Berndt, I. Sevostianov, Micromechanical analysis of the effect of void swelling on elastic and electric properties of
323 irradiated steel, *Journal of Nuclear Materials* 446 (1) (2014) 148 – 154.
- 324 [26] Z. Hashin, S. Shtrikman, A variational approach to the theory of the elastic behaviour of multiphase materials, *Journal*
325 *of the Mechanics and Physics of Solids* 11 (2) (1963) 127 – 140.
- 326 [27] V. Tvergaard, On localization in ductile materials containing spherical voids, *International Journal of Fracture* 18 (4)
327 (1982) 237–252.
- 328 [28] K. Wojtacki, P.-G. Vincent, P. Suquet, H. Moulinec, G. Boittin, A micromechanical model for the secondary creep of
329 elasto-viscoplastic porous materials with two rate-sensitivity exponents: Application to a mixed oxide fuel, *International*
330 *Journal of Solids and Structures*.
- 331 [29] T. Mori, K. Tanaka, Average stress in matrix and average elastic energy of materials with misfitting inclusions, *Acta*
332 *Metallurgica* 21 (5) (1973) 571 – 574.
- 333 [30] D. François, A. Pineau, A. Zaoui, *Mechanical behaviour of materials. Vol 1 : Micro and macroscopic constitutive behaviour,*
334 *Solid Mechanics and Its Applications*, Vol. 180, Springer, 2012.
- 335 [31] J.-B. Leblond, G. Perrin, P. Suquet, Exact results and approximate models for porous viscoplastic solids, *International*
336 *Journal of Plasticity* 10 (1994) 213–235.
- 337 [32] P. Ponte Castañeda, P. Suquet, Nonlinear composites, *Advances in Applied Mechanics* 34 (1998) 171–302.
- 338 [33] Y. Liu, P. Ponte Castañeda, Homogenization estimates for the average behavior and field fluctuations in cubic and

- 339 hexagonal viscoplastic polycrystals, *Journal of the Mechanics and Physics of Solids* 52 (2004) 1175–1211.
- 340 [34] A. L. Gurson, Continuum theory of ductile rupture by void nucleation and growth : Part I - yield criteria, *Journal of*
341 *Engineering Materials and Technology* 99 (1977) 2–15.
- 342 [35] J.-M. Gatt, Y. Monerie, D. Laux, D. Baron, Elastic behavior of porous ceramics: application to nuclear fuel materials,
343 *Journal of Nuclear Materials* 336 (2005) 145–155.
- 344 [36] M. Găărăjeu, P. Suquet, Effective properties of porous ideally plastic or viscoplastic materials containing rigid particles,
345 *Journal of the Mechanics and Physics of Solids* 45 (6) (1997) 873–902.
- 346 [37] P.-G. Vincent, P. Suquet, Y. Monerie, H. Moulinec, Effective flow surface of porous materials with two populations of
347 voids under internal pressure: II. full-field simulations, *International Journal of Plasticity* 56 (2014) 74 – 98.
- 348 [38] G. Boittin, P.-G. Vincent, H. Moulinec, M. Găărăjeu, Numerical simulations and modeling of the effective plastic flow surface
349 of a biporous material with pressurized intergranular voids, *Computer Methods in Applied Mechanics and Engineering* 323
350 (2017) 174 – 201.

351 Appendix A. Analytical model: derivations

352 Micromechanical models for the elastic properties of austenitic stainless steels subjected to radiation
353 swelling are proposed in [25]. In their work, the voids due to irradiation are considered as randomly located,
354 spherical in shape and embedded in an isotropic elastic matrix. In [25], the most widely used mean-field
355 methods in micromechanics are implemented to calculate the effective elastic properties, such as the non-
356 interaction approximation (often called dilute limit approximation), the Hashin-Shtrikman upper bound [26]
357 with the matrix as the reference medium (which coincides with the Mori-Tanaka scheme [29] in the present
358 case), the differential scheme, the self-consistent scheme (see [30] among others for a description of these
359 models). The results are compared with the experimental data of [22]. It is shown that, for the effective
360 Young modulus, all the schemes give reasonable approximation and none can be called preferential. Here,
361 following [25], we make use of the Hashin and Shtrikman upper bound to estimate the effect of voids on the
362 elastic properties of irradiated SA304L austenitic stainless steel. The overall compliance tensor is given in
363 (6).

364 The macroscopic viscoplastic strain-rate is estimated through a recent model proposed by [18] which is
365 based on the definition of a gauge surface for a porous FCC polycrystal with intragranular voids.

366 Appendix A.1. A model for porous media with isotropic viscoplastic matrix

367 First, let us recall a result from [31] in the case of an isotropic porous material with an isotropic vis-
368 coplastic matrix described by a simple Norton law of exponent n and spherical voids. In this work, the local
369 behavior of the matrix is governed by a stress potential

$$370 \dot{\epsilon}^{vp} = \frac{\partial u}{\partial \boldsymbol{\sigma}}(\boldsymbol{\sigma}) \quad \text{with} \quad u(\boldsymbol{\sigma}) = \frac{\dot{\epsilon}_0 \sigma_0}{n+1} \left(\frac{\sigma_{eq}}{\sigma_0} \right)^{n+1}, \quad (\text{A.1})$$

371 where $\dot{\epsilon}_0$ and σ_0 are constants. The macroscopic response can be characterized by an effective dissipation
372 potential \tilde{u} such that [32]

$$373 \dot{\mathbf{E}}^{vp} = \frac{\partial \tilde{u}}{\partial \boldsymbol{\Sigma}}(\boldsymbol{\Sigma}), \quad (\text{A.2})$$

374 where \tilde{u} , in the present case, is a homogeneous function of degree $n+1$ which can be written under the
375 following form

$$376 \tilde{u}(\boldsymbol{\Sigma}) = \frac{\dot{\epsilon}_0 \sigma_0}{n+1} \left(\frac{|\lambda(\boldsymbol{\Sigma})|}{\sigma_0} \right)^{n+1}. \quad (\text{A.3})$$

377 $\lambda(\boldsymbol{\Sigma})$ is a homogeneous function of degree 1 in $\boldsymbol{\Sigma}$. Gauge surfaces are equipotential surfaces used to
378 characterize the domain of statically admissible stresses. They completely characterizes the effective response
379 and they correspond to the yield surfaces in rate-independent plasticity [31]. The effective gauge surface is
380 defined as

$$\mathcal{S} = \{ \bar{\boldsymbol{\Sigma}} : \tilde{u}(\bar{\boldsymbol{\Sigma}}) = \frac{\sigma_0^{-n} \dot{\epsilon}_0}{n+1} \}. \quad (\text{A.4})$$

[31] proposed an estimate for the gauge surface under the form of equations (8) and (9). These equations
give the value of the function $\lambda(\boldsymbol{\Sigma})$ for any tensor $\boldsymbol{\Sigma}$, since the normalized tensor $\bar{\boldsymbol{\Sigma}} = \boldsymbol{\Sigma}/\lambda(\boldsymbol{\Sigma})$ belongs to
the effective gauge surface.

381 *Appendix A.2. A model for porous FCC polycrystals with intragranular voids*

382 Then, the case of a porous FCC polycrystal with intragranular spherical voids (isotropic distribution) is
 383 considered following [18]. In each grain of the polycrystal, the material surrounding the voids is governed
 384 by this stress potential ($n \geq 1$)

$$\dot{\boldsymbol{\varepsilon}}^{vp} = \frac{\partial u}{\partial \boldsymbol{\sigma}}(\boldsymbol{\sigma}) \quad \text{with} \quad u(\boldsymbol{\sigma}) = \frac{\dot{\gamma}_0 \tau_0}{n+1} \sum_{s=1}^{12} \left(\frac{|\boldsymbol{\sigma} : \boldsymbol{\mu}^{(s)}|}{\tau_0} \right)^{n+1}, \quad (\text{A.5})$$

385 where $\dot{\gamma}_0$ and τ_0 are two constants. It corresponds to a simple power law function without hardening and
 386 the corresponding viscoplastic strain rate is specified in equation (2). Since the potential u in (A.5) is still a
 387 positively homogeneous function of degree $n+1$ in $\boldsymbol{\sigma}$ (as in the previous subsection), the effective dissipation
 388 potential \tilde{u} can be written under the following form

$$\tilde{u}(\boldsymbol{\Sigma}) = \frac{\dot{\gamma}_0 \tau_0}{n+1} \left(\frac{|\lambda(\boldsymbol{\Sigma})|}{\tau_0} \right)^{n+1}, \quad (\text{A.6})$$

389 where $\lambda(\boldsymbol{\Sigma})$ is still a homogeneous function of degree 1 in $\boldsymbol{\Sigma}$. As previously, the gauge surface is defined as

$$\mathcal{S} = \{\bar{\boldsymbol{\Sigma}} : \tilde{u}(\bar{\boldsymbol{\Sigma}}) = \frac{\tau_0^{-n} \dot{\gamma}_0}{n+1}\}, \quad (\text{A.7})$$

390 and, again, an estimate of the gauge surface (A.7) leads to an estimate of the effective potential (A.6).
 391 The model proposed in [18] is based on a double up-scaling process. First, an estimate is derived for
 392 porous FCC single crystals. In this first up-scaling process, the voided single crystal is idealized as a hollow
 393 sphere assemblage (the representative volume element is idealized as an assemblage of an infinite number of
 394 homothetic hollow spheres filling up the entire volume). Then, this estimate for a porous single crystal is
 395 used together with a Voigt-type assumption (homogeneous strain rate in the polycrystal) to derive a model
 396 for the overall behavior of the polycrystal. For a purely hydrostatic loading, this model predicts that the
 397 orientation of the cubic crystal has no influence: the obtained estimate is equivalent to the estimate for the
 398 porous monocrystal under hydrostatic loading. A fully analytical gauge surface of [31] type is then derived
 399 from this result (equations (8), (9)). α is adjusted in order to match with the hydrostatic stress obtained
 400 in [19], in which the porous monocrystal was idealized as a sequential laminate of infinite rank obeying an
 401 isotropic lamination sequence. This estimate based on sequential laminates was found to be superior to
 402 more classical estimates based on hollow sphere assemblages. Then, β is adjusted in order to match with
 403 the equivalent stress obtained with the model of [33] in the case of a dense polycrystal ($f = 0$). The two
 404 up-scaling processes are presented hereafter.

405 *Appendix A.2.1. First up-scaling: porous FCC monocrystal*

406 Let us consider a representative volume element (RVE) made with a statistically uniform distribution
 407 of voids and a crystalline matrix with FCC structure. Matrix is identified as phase $r = 1$ and voids are
 408 collectively identified as phase $r = 2$. The behavior of the crystalline matrix is purely viscoplastic. The
 409 domains occupied by the crystalline matrix, the voids, and the RVE are respectively denoted by $\Omega^{(1)}$, $\Omega^{(2)}$,
 410 and Ω . The viscoplastic response of the matrix is characterized by a convex potential u such that the stress
 411 and strain rate tensors are related by (A.5). The potential u can be written under the following form

$$u(\boldsymbol{\sigma}) = \frac{\tau_0 \dot{\gamma}_0}{n+1} \sum_{s=1}^{12} \left(\frac{\boldsymbol{\sigma} : \boldsymbol{\mu}^{(s)} \otimes \boldsymbol{\mu}^{(s)} : \boldsymbol{\sigma}}{\tau_0} \right)^{(n+1)/2}, \quad (\text{A.8})$$

412 where \otimes denotes the tensor product. Alternatively, the viscoplastic behavior of the matrix can be derived
 413 from the dissipation potential w (which is the Legendre transform of u):

$$w(\dot{\boldsymbol{\varepsilon}}^{vp}) = \sup_{\boldsymbol{\sigma}} \{\boldsymbol{\sigma} : \dot{\boldsymbol{\varepsilon}}^{vp} - u(\boldsymbol{\sigma})\}. \quad (\text{A.9})$$

414 The macroscopic response (defined as the relation between the volume averages of the stress and strain-rate)
 415 can be characterized by an effective dissipation potential \tilde{w} such that (e.g. [32])

$$\Sigma = \frac{\partial \tilde{w}}{\partial \dot{\mathbf{E}}^{vp}}(\dot{\mathbf{E}}^{vp}), \quad (\text{A.10})$$

416

$$\tilde{w}(\dot{\mathbf{E}}^{vp}) = (1-f) \min_{\dot{\boldsymbol{\epsilon}}^{vp} \in \mathcal{K}(\dot{\mathbf{E}}^{vp})} \frac{1}{|\Omega^{(1)}|} \int_{\Omega^{(1)}} w(\dot{\boldsymbol{\epsilon}}^{vp}(\mathbf{x})) d\Omega. \quad (\text{A.11})$$

417 Introducing the following notation $\langle \cdot \rangle_{\Omega^{(1)}}$ for the average over $\Omega^{(1)}$, it reads

$$\tilde{w}(\dot{\mathbf{E}}^{vp}) = (1-f) \min_{\dot{\boldsymbol{\epsilon}}^{vp} \in \mathcal{K}(\dot{\mathbf{E}}^{vp})} \langle w(\dot{\boldsymbol{\epsilon}}^{vp}) \rangle_{\Omega^{(1)}}, \quad (\text{A.12})$$

418 where $f = |\Omega^{(2)}|/|\Omega|$ is the volume fraction occupied by the voids. $\mathcal{K}(\dot{\mathbf{E}}^{vp})$ is the set of kinematically
 419 admissible strain-rate fields

$$\mathcal{K}(\dot{\mathbf{E}}^{vp}) = \left\{ \dot{\boldsymbol{\epsilon}}^{vp} \in \mathcal{T} \mid \dot{\boldsymbol{\epsilon}}^{vp}(\mathbf{x}) = \nabla \otimes_s \dot{\mathbf{u}}(\mathbf{x}) \text{ in } \Omega \wedge \dot{\mathbf{u}} = \dot{\mathbf{E}}^{vp} \cdot \mathbf{x} \text{ on } \partial\Omega \right\}, \quad (\text{A.13})$$

420 where \otimes_s denotes the symmetric part of the tensor product, $\partial\Omega$ is the boundary of Ω , \mathcal{T} is the set of
 421 symmetric second-order tensors.

422 An estimate of the effective dissipation potential \tilde{w} can be obtained from (A.12) following the the approach
 423 initiated by Gurson [34]. Let us introduce the following fourth-order tensor

$$\mathbb{M} = \frac{1}{\tau_0} \sum_{s=1}^{12} \boldsymbol{\mu}^{(s)} \otimes \boldsymbol{\mu}^{(s)}. \quad (\text{A.14})$$

424 Using the following general property for a convex function $\phi(x)$ such that $\sum_{k=1}^K \lambda_k \phi(x_k) \geq \phi(\sum_{k=1}^K \lambda_k x_k)$
 425 for $\sum_{k=1}^K \lambda_k = 1$, the convex potential u can be bounded by

$$u(\boldsymbol{\sigma}) \geq u_-(\boldsymbol{\sigma}) = \frac{12 \tau_0 \dot{\gamma}_0}{n+1} \left(\frac{1}{12 \tau_0} \boldsymbol{\sigma} : \mathbb{M} : \boldsymbol{\sigma} \right)^{(n+1)/2}. \quad (\text{A.15})$$

426 When deriving this expression with respect to $\boldsymbol{\sigma}$, one gets

$$\dot{\boldsymbol{\epsilon}}^{vp} = \dot{\gamma}_0 \left(\frac{1}{12 \tau_0} \boldsymbol{\sigma} : \mathbb{M} : \boldsymbol{\sigma} \right)^{(n-1)/2} \mathbb{M} : \boldsymbol{\sigma}. \quad (\text{A.16})$$

427 Introducing \mathbb{L} the pseudo-inverse of \mathbb{M} such that $\mathbb{M} : \mathbb{L} : \mathbb{M} = \mathbb{M}$, one gets

$$\dot{\boldsymbol{\epsilon}}^{vp} : \mathbb{L} : \dot{\boldsymbol{\epsilon}}^{vp} = 12 \tau_0 \dot{\gamma}_0^2 \left(\frac{1}{12 \tau_0} \boldsymbol{\sigma} : \mathbb{M} : \boldsymbol{\sigma} \right)^n \quad (\text{A.17})$$

428 and

$$\frac{1}{12 \tau_0} \boldsymbol{\sigma} : \mathbb{M} : \boldsymbol{\sigma} = \left(\frac{1}{12 \tau_0 \dot{\gamma}_0^2} \dot{\boldsymbol{\epsilon}}^{vp} : \mathbb{L} : \dot{\boldsymbol{\epsilon}}^{vp} \right)^{1/n}. \quad (\text{A.18})$$

429 The potential u_- is homogeneous of degree $n+1$ in $\boldsymbol{\sigma}$. Thus, one can write $\boldsymbol{\sigma} : \partial_{\boldsymbol{\sigma}} u_-(\boldsymbol{\sigma}) = (n+1)u_-(\boldsymbol{\sigma})$ and
 430 $\boldsymbol{\sigma} : \dot{\boldsymbol{\epsilon}}^{vp} = (n+1)u_-(\boldsymbol{\sigma})$. Taking into account the incompressibility of the matrix together with expressions
 431 (A.18) and (A.15), the dissipation potential can be bounded by

$$w(\dot{\boldsymbol{\epsilon}}^{vp}) \leq w_+(\dot{\boldsymbol{\epsilon}}^{vp}) = \begin{cases} \frac{12 \tau_0 \dot{\gamma}_0}{m+1} \left(\frac{1}{12 \tau_0 \dot{\gamma}_0^2} \dot{\boldsymbol{\epsilon}}^{vp} : \mathbb{L} : \dot{\boldsymbol{\epsilon}}^{vp} \right)^{(m+1)/2} & \text{if } \text{tr}(\dot{\boldsymbol{\epsilon}}^{vp}) = 0 \\ +\infty & \text{otherwise} \end{cases} \quad (\text{A.19})$$

432 where $m = 1/n$. The fourth-order tensor \mathbb{M} is cubic and can be expressed in closed-form, considering the
 433 following fourth-order tensors \mathbb{I} , \mathbb{J} , \mathbb{S} with components

$$\mathbb{I}_{ijkl} = 1/2 (\delta_{ik}\delta_{jl} + \delta_{il}\delta_{jk}) \quad (\text{A.20})$$

$$\mathbb{J}_{ijkl} = 1/3 \delta_{ij}\delta_{kl} \quad (\text{A.21})$$

$$\mathbb{S}_{ijkl} = \delta_{ri}\delta_{rj}\delta_{rk}\delta_{rl}, \quad (\text{A.22})$$

436 where δ is the Kronecker symbol. \mathbb{I} is the usual fourth-order identity tensor and \mathbb{J} is the usual fourth-order
 437 projector on hydrostatic symmetric tensors of order 2. Two additional fourth-order tensors are introduced
 438 $\mathbb{K}_a = \mathbb{S} - \mathbb{J}$ and $\mathbb{K}_b = \mathbb{I} - \mathbb{S}$, so that each fourth-order cubic tensor can be decomposed into \mathbb{J} , \mathbb{K}_a , and \mathbb{K}_b .
 439 Some direct algebra leads to the following expressions for \mathbb{M} and \mathbb{L}

$$\mathbb{M} = \frac{2}{\tau_0} \mathbb{K}_a + \frac{2}{3\tau_0} \mathbb{K}_b, \quad \mathbb{L} = \frac{\tau_0}{2} \mathbb{K}_a + \frac{3\tau_0}{2} \mathbb{K}_b. \quad (\text{A.23})$$

440 Note that potential w_+ in (A.19) together with this closed form expression for \mathbb{L} is no longer explicitly
 441 dependent on the Schmid tensors. The present model follows an approach initiated in the seminal work
 442 of [34]. It consists in using the non-linear variational principle (A.11) with suitably chosen velocity fields
 443 leading to an upper bound for the effective potential. The representative volume element is considered as
 444 an assemblage of an infinite number of homothetic hollow spheres filling up the entire volume. The effective
 445 potential is bounded by using the following velocity field in any given sphere

$$\dot{\mathbf{u}}(\mathbf{x}) = \dot{E}_m \frac{b^3}{r^2} \boldsymbol{\xi} + \dot{\mathbf{E}}_d \cdot \mathbf{x}, \quad (\text{A.24})$$

446 where b is the radius of the sphere, $r = |\mathbf{x}|$, $\boldsymbol{\xi} = \mathbf{x}/|\mathbf{x}|$, and \mathbf{x} is the position vector relative to the center of
 447 the sphere. For clarity, $\dot{\mathbf{E}}^{vp}$ is replaced here by $\dot{\mathbf{E}}$. \dot{E}_m is the hydrostatic component of $\dot{\mathbf{E}}$, $\dot{E}_m = 1/3 \text{tr} \dot{\mathbf{E}}$,
 448 and $\dot{\mathbf{E}}_d$ its deviatoric part $\dot{\mathbf{E}}_d = \dot{\mathbf{E}} - \dot{E}_m \mathbf{i}$. The strain rate writes

$$\dot{\boldsymbol{\varepsilon}} = -3\dot{E}_m \frac{b^3}{r^3} \boldsymbol{\xi} \otimes_d \boldsymbol{\xi} + \dot{\mathbf{E}}_d. \quad (\text{A.25})$$

449 The effective potential is then bounded by

$$\tilde{w}(\dot{\mathbf{E}}) \leq \frac{1-f}{(4/3)\pi(b^3 - a^3)} \int_S \int_a^b w \left(-3\dot{E}_m \frac{b^3}{r^3} \boldsymbol{\xi} \otimes_d \boldsymbol{\xi} + \dot{\mathbf{E}}_d \right) r^2 dr dS(\boldsymbol{\xi}), \quad (\text{A.26})$$

450 where S is the unit sphere and a is the void radius so that $f = (a/b)^3$. Using inequality (A.19), one gets

$$\tilde{w}(\dot{\mathbf{E}}) \leq \frac{1}{(4/3)\pi b^3} \int_S \int_a^b w_+ \left(-3\dot{E}_m \frac{b^3}{r^3} \boldsymbol{\xi} \otimes_d \boldsymbol{\xi} + \dot{\mathbf{E}}_d \right) r^2 dr dS(\boldsymbol{\xi}) \quad (\text{A.27})$$

451 or

$$\tilde{w}(\dot{\mathbf{E}}) \leq \frac{1}{(4/3)\pi b^3} \int_S \int_a^b \frac{12\tau_0\dot{\gamma}_0}{m+1} \left(\frac{1}{12\tau_0\dot{\gamma}_0^2} \dot{\boldsymbol{\varepsilon}} : \mathbb{L} : \dot{\boldsymbol{\varepsilon}} \right)^{(m+1)/2} r^2 dr dS(\boldsymbol{\xi}). \quad (\text{A.28})$$

452 This right hand expression is then bounded by applying the Cauchy-Schwarz inequality to this surface
 453 integral

$$\tilde{w}(\dot{\mathbf{E}}) \leq \frac{1}{(4/3)\pi b^3} \int_a^b (4\pi)^{(1-m)/2} \frac{12\tau_0\dot{\gamma}_0}{m+1} \left(\int_S \frac{1}{12\tau_0\dot{\gamma}_0^2} \dot{\boldsymbol{\varepsilon}} : \mathbb{L} : \dot{\boldsymbol{\varepsilon}} dS(\boldsymbol{\xi}) \right)^{(m+1)/2} r^2 dr. \quad (\text{A.29})$$

454 By using the velocity field (A.25), in this expression, one gets

$$\tilde{w}(\dot{\mathbf{E}}) \leq \frac{12\tau_0\dot{\gamma}_0}{m+1} \int_f^1 \left(\frac{1}{12\tau_0\dot{\gamma}_0^2} 9\dot{E}_m^2 \frac{\kappa}{y^2} + \frac{1}{12\tau_0\dot{\gamma}_0^2} \dot{\mathbf{E}}^d : \mathbb{L} : \dot{\mathbf{E}}^d \right)^{(m+1)/2} dy, \quad (\text{A.30})$$

455 where $\kappa = (11/15)\tau_0$.

456 *Appendix A.2.2. Second up-scaling: polycrystal*

457 In the second transition of scales, the domain Ω consists of the polycrystal idealized as an heterogeneous
 458 material with N phases (domains $\Omega^{(r)}$, volume fractions $c^{(r)}$) described by the overall behavior of a porous
 459 single crystal. Random orientation is considered for each phase of the polycrystal. The local potential $w^{(r)}$
 460 in each phase r is obtained by the first scale transition and corresponds to the right hand side in expression
 461 (A.30). As before, the effective strain rate potential reads

$$\tilde{w}(\dot{\mathbf{E}}) = \min_{\dot{\boldsymbol{\varepsilon}} \in \mathcal{K}(\dot{\mathbf{E}})} \sum_{r=1}^N c^{(r)} \left\langle w^{(r)}(\dot{\boldsymbol{\varepsilon}}) \right\rangle_{\Omega^{(r)}}. \quad (\text{A.31})$$

462 Using a Voigt-type assumption (homogeneous strain rate in the whole volume), one gets

$$\tilde{w}(\dot{\mathbf{E}}) \leq \sum_{r=1}^N c^{(r)} \left\langle w^{(r)}(\dot{\mathbf{E}}) \right\rangle_{\Omega^{(r)}}. \quad (\text{A.32})$$

463 Note that, in this expression, the tensor $\dot{\mathbf{E}}$ has to be expressed in the local basis of each phase r . For any
 464 phase r , there is a second order tensor $\mathbf{Q}^{(r)}$ such that

$$w^{(r)}(\dot{\mathbf{E}}) = w^{(0)}(\mathbf{Q}^{(r)} \cdot \dot{\mathbf{E}} \cdot (\mathbf{Q}^{(r)})^T), \quad (\text{A.33})$$

465 where

$$w^{(0)}(\dot{\boldsymbol{\varepsilon}}) = \frac{12\tau_0\dot{\gamma}_0}{m+1} \int_f^1 \left(\frac{1}{12\tau_0\dot{\gamma}_0^2} 9\dot{\boldsymbol{\varepsilon}}_m^2 \frac{\kappa}{y^2} + \frac{1}{12\tau_0\dot{\gamma}_0^2} \dot{\boldsymbol{\varepsilon}}^d : \mathbb{L} : \dot{\boldsymbol{\varepsilon}}^d \right)^{(m+1)/2} dy. \quad (\text{A.34})$$

466 For a statistically uniform distribution of grains and for an infinity number of grains, the representative
 467 volume element can be considered as a spherical in shape volume in which each point corresponds to a
 468 grain. Then (A.32) can be evaluated by an integration over the unit sphere S such that

$$\tilde{w}(\dot{\mathbf{E}}) \leq \left\langle w^{(0)}(\mathbf{Q} \cdot \dot{\mathbf{E}} \cdot \mathbf{Q}^T) \right\rangle_S, \quad (\text{A.35})$$

469 where the following notation is used $\langle x \rangle_S = 1/(4\pi) \int_S x dS$. One gets

$$\tilde{w}(\dot{\mathbf{E}}) \leq \frac{\tau_0\dot{\gamma}_0}{m+1} \int_f^1 \left\langle \left(\frac{1}{\dot{\gamma}_0^2} 9\dot{\mathbf{E}}_m^2 \frac{\kappa^*}{y^2} + \frac{1}{\dot{\gamma}_0^2} \dot{\mathbf{E}}^d(\mathbf{Q}) : \mathbb{L}^* : \dot{\mathbf{E}}^d(\mathbf{Q}) \right)^{(m+1)/2} \right\rangle_S dy, \quad (\text{A.36})$$

470 where $\kappa^* = (12^{(1-m)/(m+1)}/\tau_0)\kappa$ and $\mathbb{L}^* = (12^{(1-m)/(m+1)}/\tau_0)\mathbb{L}$. Then the Cauchy-Schwarz inequality is
 471 applied

$$\tilde{w}(\dot{\mathbf{E}}) \leq \frac{\tau_0\dot{\gamma}_0}{m+1} \int_f^1 \left(\frac{1}{\dot{\gamma}_0^2} 9\dot{\mathbf{E}}_m^2 \frac{\kappa^*}{y^2} + \frac{1}{\dot{\gamma}_0^2} \left\langle \dot{\mathbf{E}}^d(\mathbf{Q}) : \mathbb{L}^* : \dot{\mathbf{E}}^d(\mathbf{Q}) \right\rangle_S \right)^{(m+1)/2} dy. \quad (\text{A.37})$$

472 Then, considering $\dot{\mathbf{E}}^d(\mathbf{Q}) : \mathbb{L}^* : \dot{\mathbf{E}}^d(\mathbf{Q}) = \dot{\mathbf{E}}^d : \mathbb{L}^*(\mathbf{Q}) : \dot{\mathbf{E}}^d$ together with a result from [35] to get the
 473 orientation average of a fourth order tensor, one gets

$$\left\langle \dot{\mathbf{E}}^d : \mathbb{L}^*(\mathbf{Q}) : \dot{\mathbf{E}}^d \right\rangle_S = \frac{33}{20} 12^{(1-m)/(m+1)} \dot{\mathbf{E}}_{eq}^2, \quad (\text{A.38})$$

474 where $\dot{\mathbf{E}}_{eq} = \sqrt{2/3 \dot{\mathbf{E}}^d : \dot{\mathbf{E}}^d}$. Then (A.37) writes

$$\tilde{w}(\dot{\mathbf{E}}) \leq \frac{\tau_0\dot{\gamma}_0}{m+1} \int_f^1 \left(\frac{1}{\dot{\gamma}_0^2} 9\dot{\mathbf{E}}_m^2 \frac{\kappa^*}{y^2} + \frac{1}{\dot{\gamma}_0^2} q^* \dot{\mathbf{E}}_{eq}^2 \right)^{(m+1)/2} dy, \quad (\text{A.39})$$

475 where $q^* = (33/20)12^{(1-m)/(m+1)}$.

476 *Appendix A.2.3. Derivation of a gauge surface*

477 In the case of perfect plasticity ($m \rightarrow 0$), the inequality (A.39) writes

$$W(\dot{\mathbf{E}}) \leq \tau_0 \int_f^1 \left(9\dot{E}_m^2 \frac{\kappa^*}{y^2} + q^* \dot{E}_{eq}^2 \right)^{1/2} dy. \quad (\text{A.40})$$

478 The yield surface associated with this effective strain-rate potential writes

$$\frac{1}{q^*} \left(\frac{\Sigma_{eq}}{\tau_0} \right)^2 + 2f \cosh \left(\frac{1}{\sqrt{\kappa^*}} \frac{\Sigma_m}{\tau_0} \right) - 1 - f^2 = 0. \quad (\text{A.41})$$

479 This result can be found directly by using a lemma given in [36] (Appendix A). By analogy with the
480 work of [31] it is then proposed to extend this yield surface in plasticity to the following gauge surface in
481 viscoplasticity

$$\frac{1}{q^*} \frac{\Sigma_{eq}^2}{\lambda^2} + f \left(h^* \left(\frac{\Sigma_m}{\lambda} \right) + \frac{n-1}{n+1} (h^*)^{-1} \left(\frac{\Sigma_m}{\lambda} \right) \right) - 1 - \frac{n-1}{n+1} f^2 = 0, \quad (\text{A.42})$$

482 where

$$h^*(x) = \left(1 + \frac{1}{n} \left| \frac{1}{\sqrt{\kappa^*}} x \right|^{1+\frac{1}{n}} \right)^n. \quad (\text{A.43})$$

483 Accurate homogenization estimates are already available for two particular cases: fully dense polycrystals
484 under pure shear loadings [33], and porous polycrystals under pure hydrostatic loadings [19]. As it stands,
485 the above gauge surface does not recover those accurate estimates, but it can be easily modified to do so.
486 First, the coefficient κ^* entering h^* is adjusted in order to match with the hydrostatic stress predicted by
487 the homogenization estimate of [19], in which the porous monocrystal was idealized as a sequential laminate
488 of infinite rank obeying an isotropic lamination sequence. This estimate based on sequential laminates was
489 found to be superior to more classical estimates based on hollow sphere assemblages. Second, q^* is adjusted
490 in order to match with the shear stress predicted by the linear-comparison homogenization model of [33] for
491 fully dense polycrystals ($f = 0$). In conclusion, the gauge surface is expressed as

$$\left(\frac{1}{\tilde{\sigma}_0/\tau_0} \right)^{2n/(n+1)} \frac{\Sigma_{eq}^2}{\lambda^2} + f \left(h^{**} \left(\frac{\Sigma_m}{\lambda} \right) + \frac{n-1}{n+1} (h^{**})^{-1} \left(\frac{\Sigma_m}{\lambda} \right) \right) - 1 - \frac{n-1}{n+1} f^2 = 0, \quad (\text{A.44})$$

492 where

$$h^{**}(x) = \left(1 + \frac{1}{n} \frac{1}{\alpha_{LAM}/\tau_0} |x|^{1+\frac{1}{n}} \right)^n. \quad (\text{A.45})$$

493 For simplicity, α_{LAM}/τ_0 and $(\tilde{\sigma}_0/\tau_0)^{2n/(n+1)}$ are respectively denoted by α and β in equations (8) and (9).
494 Thus function h^{**} coincides with function h (equation (9)). Equations (A.2) and (A.6) give

$$\dot{\mathbf{E}}^{vp} = \dot{\gamma}_0 \left(\frac{|\lambda|}{\tau_0} \right)^n \text{sign}(\lambda) \frac{\partial \lambda}{\partial \Sigma}. \quad (\text{A.46})$$

495 The definition of the gauge surface (A.7) together with this relation

$$\frac{\partial \mathcal{S}}{\partial \Sigma} \frac{\partial \bar{\Sigma}}{\partial \Sigma} = 0, \quad (\text{A.47})$$

496 lead to the following equality

$$\frac{\partial \lambda}{\partial \Sigma} = \frac{\lambda}{\Sigma} \frac{\partial \mathcal{S}}{\partial \Sigma}. \quad (\text{A.48})$$

497 Thus, equation (A.46) writes

$$\dot{\mathbf{E}}^{vp} = \dot{\gamma}_0 \left(\frac{|\lambda|}{\tau_0} \right)^n \frac{1}{\Sigma} \frac{\partial \mathcal{S}}{\partial \Sigma} \text{sign}(\lambda). \quad (\text{A.49})$$

498 By writing

$$\frac{\partial \mathcal{S}}{\partial \boldsymbol{\Sigma}} = \frac{1}{3} \frac{\partial \mathcal{S}(\bar{\boldsymbol{\Sigma}}_m \mathbf{i})}{\partial \bar{\boldsymbol{\Sigma}}_m} \mathbf{i} + \frac{\partial \mathcal{S}(\bar{\boldsymbol{\Sigma}}_d)}{\partial \bar{\boldsymbol{\Sigma}}_d} \quad (\text{A.50})$$

499 and

$$\frac{\partial \mathcal{S}(\bar{\boldsymbol{\Sigma}}_m \mathbf{i})}{\partial \bar{\boldsymbol{\Sigma}}_m} = f \left(h^{**'}(\bar{\boldsymbol{\Sigma}}_m) - \frac{n-1}{n+1} (h^{**})^{-2}(\bar{\boldsymbol{\Sigma}}_m) h^{**'}(\bar{\boldsymbol{\Sigma}}_m) \right), \quad (\text{A.51})$$

$$\frac{\partial \mathcal{S}(\bar{\boldsymbol{\Sigma}}_d)}{\partial \bar{\boldsymbol{\Sigma}}_d} = 3 \left(\frac{1}{\bar{\sigma}_0/\tau_0} \right)^{2n/(n+1)} \bar{\boldsymbol{\Sigma}}_d, \quad (\text{A.52})$$

$$h^{**'}(x) = \frac{1}{\alpha_{LAM}/\tau_0} \frac{n+1}{n} \left(1 + \frac{1}{\alpha_{LAM}/\tau_0} \frac{1}{n} |x|^{1+\frac{1}{n}} \right)^{n-1} |x|^{\frac{1}{n}} \text{sign}(x), \quad (\text{A.53})$$

502 it leads to equation (5).

503 Appendix A.3. Time-integration of the micromechanical model

504 In closed form, the analytical model presented in 2.3 writes

$$\dot{\boldsymbol{\Sigma}} = \tilde{\mathbf{C}} : \left(\hat{\mathbf{E}} - \dot{\gamma}_0 \left| \frac{\lambda}{\tau_0} \right|^n \frac{f \left(1 - \frac{n-1}{n+1} h^{-2}(\Sigma_m/\lambda) \right) |h'(\Sigma_m/\lambda)| \text{sign}(\Sigma_m) \mathbf{i} + \frac{3}{\beta} (\boldsymbol{\Sigma}_d/|\lambda|)}{f \left(1 - \frac{n-1}{n+1} h^{-2}(\Sigma_m/\lambda) \right) |h'(\Sigma_m/\lambda)| |\Sigma_m/\lambda| + \frac{2}{\beta} (\Sigma_{eq}/\lambda)^2} \right) \quad (\text{A.54})$$

505 with $\tilde{\mathbf{C}} = \tilde{\mathbf{S}}^{-1}$. This equation can be written under the form $\dot{\mathbf{Y}} = F(\mathbf{Y}, \hat{\mathbf{E}})$ where \mathbf{Y} is a vector containing
 506 the stress $\boldsymbol{\Sigma}$. For a time increment ΔT , vector \mathbf{Y} is updated by a Runge-Kutta (3)2 FSAL (First Same As
 507 Last) method. Tolerance factor ε is set to 10^{-5} . General algorithm writes

508 • Initialization $\mathbf{k}_{FSAL} = F(\mathbf{Y}_0)$, $\delta t = \Delta T$, $\Delta t = 0$, $p = 0$

509 • While $\Delta t < \Delta T$ do

510 1. Evaluate \mathbf{Y}_{p+1} by a Runge-Kutta method with order 3

$$511 \quad \mathbf{k}_1 = \mathbf{k}_{FSAL}$$

$$512 \quad \mathbf{k}_2 = F(\mathbf{Y}_p + \bar{a}_{21} \mathbf{k}_1 \delta t)$$

$$513 \quad \mathbf{k}_3 = F(\mathbf{Y}_p + \bar{a}_{31} \mathbf{k}_1 \delta t + \bar{a}_{32} \mathbf{k}_2 \delta t)$$

$$514 \quad \mathbf{Y}_{p+1} = \mathbf{Y}_p + (\bar{b}_1 \mathbf{k}_1 + \bar{b}_2 \mathbf{k}_2 + \bar{b}_3 \mathbf{k}_3) \delta t$$

515 2. Evaluate $\hat{\mathbf{Y}}_{p+1}$ by a Runge-Kutta method with order 2

$$516 \quad \mathbf{k}_{FSAL} = F(\mathbf{Y}_{p+1})$$

$$517 \quad \hat{\mathbf{Y}}_{p+1} = \mathbf{Y}_p + (\bar{d}_1 \mathbf{k}_1 + \bar{d}_2 \mathbf{k}_2 + \bar{d}_3 \mathbf{k}_3 + \bar{d}_4 \mathbf{k}_{FSAL}) \delta t$$

518 3. Evaluate the relative error η between the 2 methods

$$519 \quad \eta = \max_i \left(|Y_{p+1}^{(i)} - \hat{Y}_{p+1}^{(i)}| / |Y_{p+1}^{(i)}| + 10^{-20} \right) \text{ where } Y^{(i)} \text{ denotes the } i\text{-th component for } \mathbf{Y}$$

520 4. Convergence criterion

521 if $\eta \leq \varepsilon$ then

$$522 \quad \mathbf{Y}_p := \mathbf{Y}_{p+1}$$

$$523 \quad \Delta t := \Delta t + \delta t$$

$$524 \quad p := p + 1$$

525 endif

526 5. Evaluate the optimal time step δt

527 if $\eta \leq \varepsilon$ then

528 $\delta t_{opt} = \min \left(2, (\varepsilon/\eta)^{1/3} \right) \delta t$
529 else
530 $\delta t_{opt} = \max \left(1/2, 0.9 (\varepsilon/\eta)^{1/3} \right) \delta t$
531 endif
532 $\delta t = \min (\delta t_{opt}, \Delta T - \Delta t)$

533 • end

534 where coefficients \bar{a}_{ij} , \bar{b}_j and \bar{d}_j are defined as $\bar{a}_{21} = 1/2$, $\bar{a}_{31} = 0$, $\bar{a}_{32} = 3/4$, $\bar{b}_1 = 2/9$, $\bar{b}_2 = 1/3$, $\bar{b}_3 = 4/9$,
535 $\bar{d}_1 = 7/24$, $\bar{d}_2 = 1/4$, $\bar{d}_3 = 1/3$ and $\bar{d}_4 = 1/8$. During the algorithm, when function F needs to be evaluated,
536 the scalar $|\lambda|$ is obtained by solving the non linear equation (8) by a Newton method. Particular care must
537 be taken when initializing the Newton algorithm. Equation (8) can be written under the following form

$$\frac{1}{\beta} (\Sigma_{eq}/\lambda)^2 + f \sqrt{\frac{n-1}{n+1}} \left(\sqrt{\frac{n+1}{n-1}} h(\Sigma_m/\lambda) + \sqrt{\frac{n-1}{n+1}} h^{-1}(\Sigma_m/\lambda) \right) - 1 - \frac{n-1}{n+1} f^2 = 0. \quad (\text{A.55})$$

538 The inequality $x + 1/x \geq 2$ when $x \geq 0$ allows to write the following inequality ($\beta \geq 0$)

$$|\lambda| \geq |\lambda_0| = \frac{\Sigma_{eq}}{\sqrt{\beta} |1 - f \sqrt{\frac{n-1}{n+1}}|}. \quad (\text{A.56})$$

539 Newton algorithm is initialized using this lower bound for $|\lambda|$. Note also that the purely hydrostatic case
540 ($\Sigma_{eq} = 0$) leads to the straightforward solution for $|\lambda|$

$$|\lambda| = \left(\alpha n \left(f^{-1/n} - 1 \right) \right)^{-n/(n+1)} |\Sigma_m|. \quad (\text{A.57})$$

541 Similarly, the purely deviatoric case ($\Sigma_m = 0$) leads to the straightforward solution for $|\lambda|$

$$|\lambda| = \frac{\Sigma_{eq}}{\sqrt{\beta} \left(1 + \frac{n-1}{n+1} f^2 \right)}. \quad (\text{A.58})$$

542 To the end, Newton algorithm writes

543 • From \mathbf{Y} , compute the absolute value of the stress triaxiality $X_{\Sigma} = |\Sigma_m|/\Sigma_{eq}$, compute $|\lambda_0|$ with
544 equation (A.56)

545 • if $X_{\Sigma} > 10^5$ then evaluate $|\lambda|$ from the purely hydrostatic solution (A.57), endif and exit.

546 • if $X_{\Sigma} < 10^{-5}$ then evaluate $|\lambda|$ from the purely deviatoric solution (A.58), endif and exit.

547 • while $q < 1000$, do

548 $\lambda_q := \lambda_{q+1}$

549 $\lambda_{q+1} = \lambda_q - \mathcal{S}(\lambda_q) / \partial_{\lambda_q} \mathcal{S}(\lambda_q)$

550 Convergence criterion

551 if $|\lambda_{q+1} - \lambda_q| - TOL < 0$ then $|\lambda| = |\lambda_{q+1}|$ exit

552 else $q := q + 1$ endif

553 • end

554 The derivative $\partial_{\lambda} \mathcal{S}(\lambda)$ writes

$$\frac{\partial \mathcal{S}}{\partial \lambda}(\lambda) = -\frac{2}{\beta} \frac{(\Sigma_{eq})^2}{\lambda^3} - f \frac{\Sigma_m}{\lambda^2} \left(h'(\Sigma_m/\lambda) - \frac{n-1}{n+1} h^{-2}(\Sigma_m/\lambda) h'(\Sigma_m/\lambda) \right). \quad (\text{A.59})$$

$\mathbf{n}^{(s)}$	(111)			$(\bar{1}\bar{1}\bar{1})$			$(\bar{1}\bar{1}\bar{1})$			$(\bar{1}\bar{1}\bar{1})$		
$\mathbf{m}^{(s)}$	$[0\bar{1}\bar{1}]$	$[10\bar{1}]$	$[1\bar{1}0]$	$[0\bar{1}\bar{1}]$	$[101]$	$[110]$	$[011]$	$[101]$	$[1\bar{1}0]$	$[011]$	$[10\bar{1}]$	$[110]$

Table A.5: Slip systems for face-centered cubic crystals with Schmid and Boas notations.

k	1	2	3	4	5	6	7	8	9	10	11	12
1	a_1	a_2	a_2	a_4	a_5	a_5	a_5	a_6	a_3	a_5	a_3	a_6
2	a_2	a_1	a_2	a_5	a_3	a_6	a_4	a_5	a_5	a_5	a_6	a_3
3	a_2	a_2	a_1	a_5	a_6	a_3	a_5	a_3	a_6	a_4	a_5	a_5
4	a_1	a_5	a_5	a_1	a_2	a_2	a_6	a_5	a_3	a_6	a_3	a_5
5	a_5	a_3	a_6	a_2	a_1	a_2	a_3	a_5	a_6	a_5	a_5	a_4
6	a_5	a_6	a_3	a_2	a_2	a_1	a_5	a_4	a_5	a_3	a_6	a_5
7	a_5	a_4	a_5	a_6	a_3	a_5	a_1	a_2	a_2	a_6	a_5	a_3
8	a_6	a_5	a_3	a_5	a_5	a_4	a_2	a_1	a_2	a_3	a_3	a_6
9	a_3	a_5	a_6	a_3	a_6	a_5	a_3	a_2	a_1	a_5	a_4	a_5
10	a_5	a_5	a_4	a_6	a_5	a_3	a_6	a_3	a_5	a_1	a_2	a_3
11	a_3	a_6	a_5	a_3	a_5	a_6	a_5	a_5	a_4	a_2	a_1	a_2
12	a_6	a_3	a_5	a_5	a_4	a_5	a_3	a_6	a_5	a_2	a_2	a_1

Table A.6: General form of the dislocation interaction matrix \mathbf{a} .

555 *Appendix A.4. Slip systems*

556 Unit vectors $\mathbf{n}^{(s)}$ and $\mathbf{m}^{(s)}$ used to define the Schmid tensors $\boldsymbol{\mu}^{(s)}$ are recalled in Table A.5.

557 *Appendix A.5. Dislocation interaction matrix \mathbf{a}*

558 The dislocation interaction matrix \mathbf{a} writes under the form specified in Table A.6.

559 **Appendix B. Numerical model: parametric studies**

560 *Appendix B.1. Statistical representativeness*

561 A parametric study has been carried out in order to determine the number of grains within a unit cell
562 required for statistical representativeness. This is a difficult issue that cannot be addressed thoroughly. First,
563 it is clear that the notion of representativeness is an asymptotic notion (the exact representativeness can only
564 be reached for an infinite medium) and secondly, it depends on the “quantity of interest”. Here, stationarity
565 is only studied for the effective tensile curve, and particularly for the maximal overall stress. Computations
566 are performed on cells with 64^3 , 128^3 , 256^3 and 512^3 voxels. The mean number of voxels per grain is fixed to
567 32^3 . By doing so, a cell with 8 grains contains 64^3 voxels, 64 grains leads to 128^3 voxels, 512 grains leads to
568 256^3 voxels, 4096 grains leads to 512^3 voxels. For each case, 10 realizations of microstructures are drawn as
569 depicted on Figure B.14, B.15, and B.16, except for the case with 4096 grains (512^3 voxels), for which only
570 one microstructure is considered (Figure B.17). The tensile curves obtained from these microstructures are
571 shown in Figure B.18: only one case per volume size is reported here, as the same trend has been observed
572 with the other realizations. The simulations are performed using the parameters reported in Table 3 along
573 with the values $\bar{\gamma}_0 = 0.5$ and $\bar{\tau}_0 = 58$ MPa determined in Section 4. The overall maximal stress R_m versus
574 the number of grains in the cells is plotted in Figure B.19. One can observe that dispersion is low when 512
575 grains are considered. Thus, these figures tend to indicate that a single realization with 512 grains in the
576 aggregate seems to be a good compromise between size and accuracy.

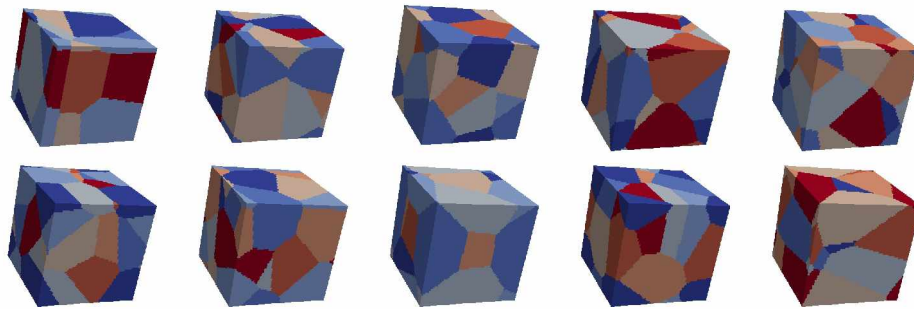


Figure B.14: 10 different microstructures considered for the statistical representativeness study. 8 grains in each cell.

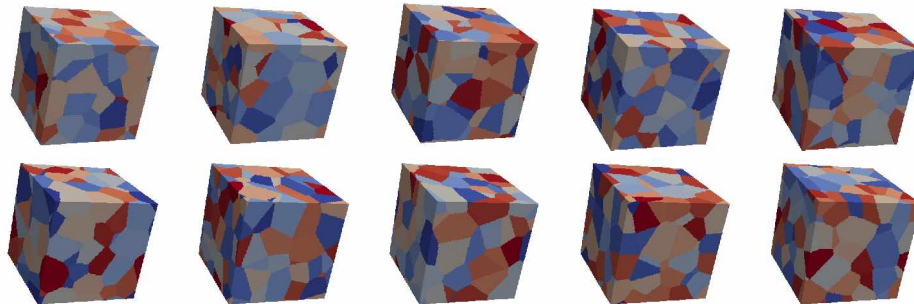


Figure B.15: 10 different microstructures considered for the statistical representativeness study. 64 grains in each cell.

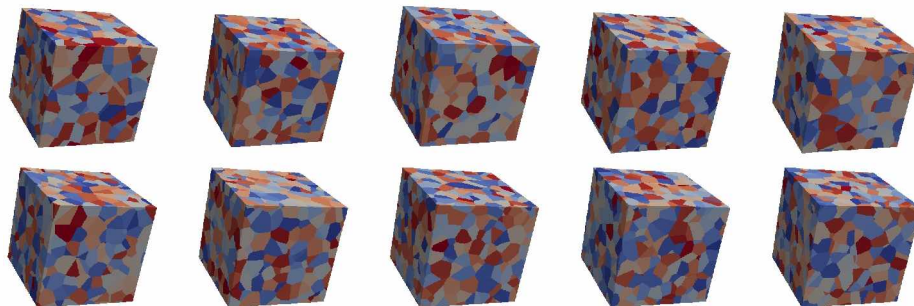


Figure B.16: 10 different microstructures considered for the statistical representativeness study. 512 grains in each cell.

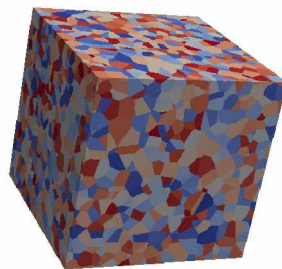


Figure B.17: Microstructure with 4096 grains considered for the statistical representativeness study.

577 *Appendix B.2. Spatial resolution*

578 A second parametric study has been carried out in order to determine a suitable spatial discretization
 579 (in voxels) of the microstructures. This parameter is closely related to the number of voxels which should

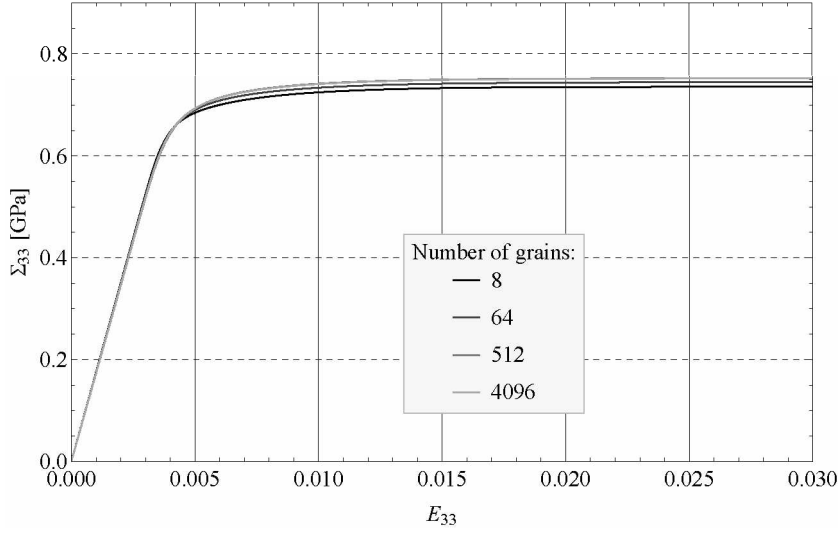


Figure B.18: Simulated tensile curves. Effect of the number of grains in the cell. Simulations performed on the top left microstructures of Figure B.14 with 8 grains, Figure B.15 with 64 grains, Figure B.16 with 512 grains and the microstructure of Figure B.17 with 4096 grains.

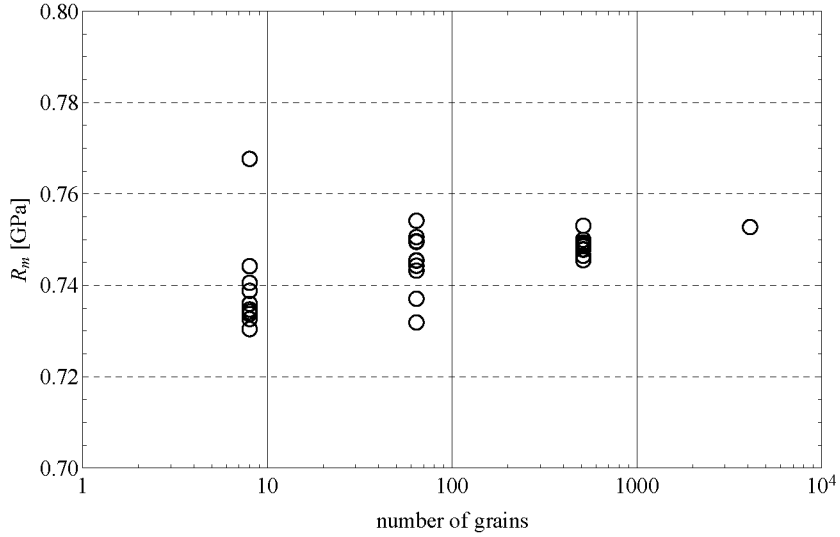


Figure B.19: Maximal overall stress obtained from the simulated tensile curves. Effect of the number of grains in the cell. Simulations performed on the microstructures of Figure B.14 with 8 grains, Figure B.15 with 64 grains, Figure B.16 with 512 grains and the microstructure of Figure B.17 with 4096 grains.

580 be used for each grain of the aggregate in order to capture the field fluctuations in each grain leading to
 581 an accurate overall response of the aggregate. A specific microstructure with 100 grains is considered. The
 582 number of voxels used in its spatial discretization is increasing as shown in Figure B.20. Once again, the
 583 simulations are performed using the set of parameters reported in Table 3 along with $\bar{\gamma}_0 = 0.5$ and $\bar{\tau}_0 = 58$
 584 MPa.

585 The simulated tensile curves are shown in Figure B.21. A very good agreement between the different
 586 cases is observed: all curves superimpose almost perfectly. Then, the question of spatial discretization of the
 587 microstructures in the porous case is addressed. The question is closely related to the number of voxels which
 588 should be used for each intragranular void inside the aggregate. As explained in [37], this question should

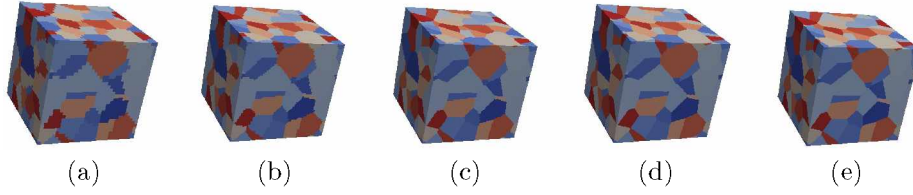


Figure B.20: For the same microstructure, increase of the number of voxels used for the spatial discretization: (a) 32^3 voxels, (b) 64^3 voxels, (c) 128^3 voxels, (d) 256^3 voxels, (e) 512^3 voxels.

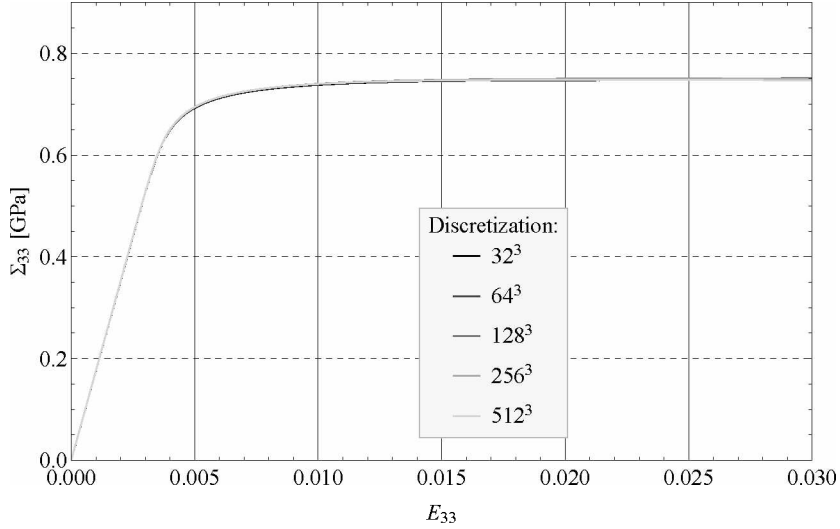


Figure B.21: Simulated tensile curves. Effect of the number of voxels (discretization). Simulations performed on the microstructures of Figure B.20 with 100 grains.

589 be addressed, ideally, realization by realization, by conducting parametric studies in which the number of
590 voxels is increased until stationarity of the quantities of interest (here the maximal overall stress) is reached.
591 Following this procedure would require a formidable computational effort in the porous polycrystal case
592 where we want to put as many as possible of the smallest possible voids inside the grains with respect to the
593 available RAM memory. To fix ideas, a simulation with 512^3 voxels already requires 140 GB RAM. Instead
594 of that, we followed a procedure already implemented in past studies [37, 38, 28] which consists in examining
595 a cubic unit-cell with a single void at its center and determining how many voxels are required to achieve
596 a reasonable compromise for a single void. The porosity is set to 4% and a study relative to the spatial
597 discretization is performed. The microstructures are plotted on Figure B.22. The crystal surrounding the
598 void is oriented along the laboratory basis (Euler angles $(\phi_1, \Phi, \phi_2) = (0, 0, 0)$). For each discretization, the
599 obtained tensile curve is plotted in Figure B.23. This figure tends to indicate that the discretization with
600 32^3 voxels is a good compromise between size and accuracy. It corresponds to a number of 1310 voxels per
601 void. In Section 3 we adopt a discretization with 512^3 voxels so as not to increase too much the amount of
602 required memory. For each porous microstructure, the porosity and the number of voids are specified to get
603 approximately 1310 voxels per void.

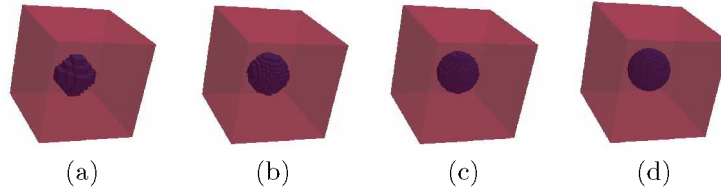


Figure B.22: For the same microstructure, increase of the number of voxels used for the spatial discretization (porous case, single void): (a) 16^3 voxels, (b) 32^3 voxels, (c) 64^3 voxels, (d) 128^3 voxels.

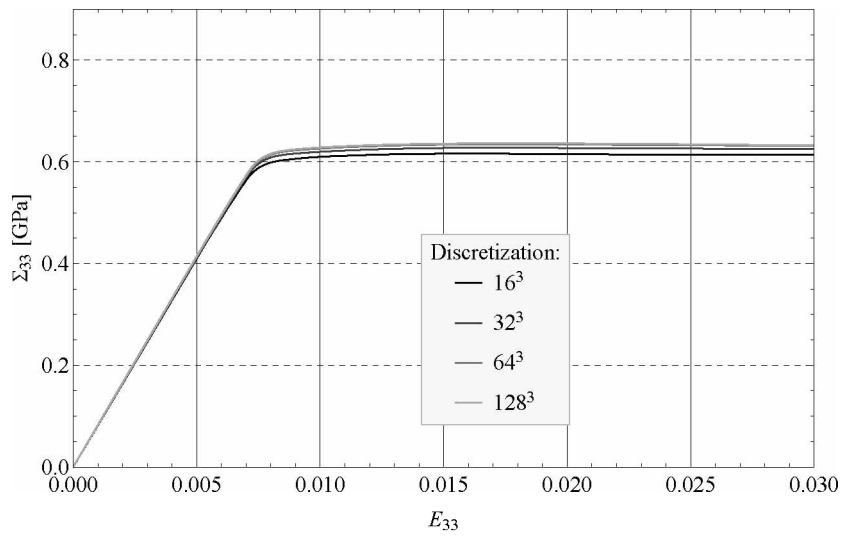


Figure B.23: Simulated tensile curves for porous monocystal with the microstructures displayed in Figure B.22. Effect of the number of voxels (discretization).